

Fig. 1 Fluorescent presentation of ex vivo gene transfection with gelatin-DNA complex in macrophages/monocytes as well as fibroblasts. Rat macrophages (A and B) and human monocytes (C and D) were cultured with gelatin-GFP-gene complex for 14 days. Transmittance microscopic images (A and C) and fluorescence images (B and D) of the cells are shown. Macrophages (B) and monocytes (D) show fluorescence due to GFP. Arrowheads indicate GFP-expressing cells. Arrows indicate gelatin particles themselves. Bars = 20 μ m

Organ distribution of phagocytes injected intravenously or directly into ischemic muscle

We studied quantitatively whether intravenously injected luciferase-gene-transfected phagocytes could target ischemic tissues (the third and fifth columns from the left in Table 1). In non-ischemic rats, the injected macrophages were recognized almost exclusively in the spleen ($98 \pm 4\%$) ($n = 7$, the second column in Table 1). In non-ischemic mice, similar results were observed ($n = 7$, data not shown). In a rat with myocardial ischemia-reperfusion injury, some of the intravenously injected macrophages were incorporated into the heart (the third column in Table 1). The incorporation into the post-ischemic pericardium amounted to $13 \pm 6\%$ ($n = 7$) (non-ischemic rats $0 \pm 0\%$, $n = 7$, Table 1). The incorpo-

rated cells expressed GFP (Fig. 3). Fibrosis with inflammatory infiltrates was recognized in the anterior wall of the left ventricle, extending to the interventricular septum (Figs. 3A and B). These infiltrates were mainly polymorphonuclear leukocytes and macrophages (Figs. 3C and D). Approximately 20% of the macrophages showed GFP-positivity in this area (Figs. 3E and F). Similar tissue-targeting by intravenously injected monocytes was confirmed in a mouse model with hindlimb ischemia ($13 \pm 7\%$, $n = 7$, the fifth column in Table 1). Furthermore, we studied whether local intramuscular injection increased the degree of tissue targeting (the fourth and sixth columns from the left in Table 1). After direct injection of phagocytes into ischemic muscle, $86 \pm 10\%$ and $88 \pm 6\%$ of the cells remained in the target tissue in the two models. Thirteen and 11% of phagocytes in-

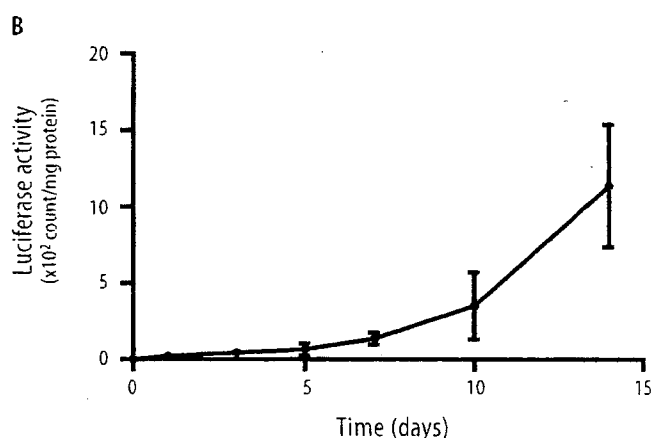
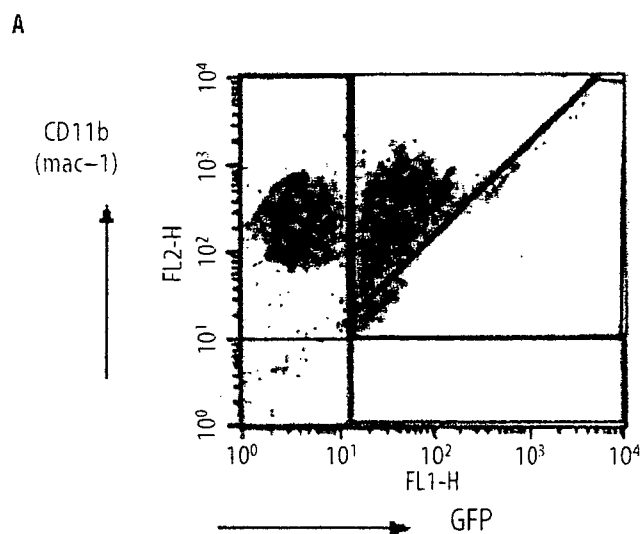


Fig. 2 Quantitative assessment of gene transfection into rat macrophages. (A) Fluorescence-activated cell sorting analysis of transfected macrophages done on day 14 of culture with reference to GFP-positive and Mac1-positive cells. (B) Sequential changes of luciferase activity in cultured macrophages in the presence of luciferase-gene-gelatin complex. Values are mean \pm SD. The number of experiments is shown in parentheses

jected into the cardiac or hindlimb muscle migrated to the spleen. In the other organs, accumulation of phagocytes were negligible.

Amelioration of ischemia by intravenously injected angiogenic-gene-transfected phagocytes

In the rat model with myocardial ischemia-reperfusion injury, we studied the angiogenic effect of intravenously injected macrophages transfected with fibroblast growth factor 4 (FGF4) gene by using gelatin. Intravenous injection of these macrophages (1.0×10^6) significantly increased the regional blood flow in the ischemic myocardium ($78 \pm 7.1\%$, $n = 8$, in terms of flow ratio of

Table 1 Organ distribution of phagocytes injected into the vein and into local tissue

| Organ | Normal i.v. (7 rats) | Myocardial injury i.v. (7 rats) | Myocardial injury i.m. (7 rats) | Hindlimb ischemia i.v. (7 mice) | Hindlimb ischemia i.m. (7 mice) |
|-----------------|----------------------|---------------------------------|---------------------------------|---------------------------------|---------------------------------|
| Heart | 0 \pm 0 | 13 \pm 6 | 86 \pm 10 | 0 \pm 0 | 0 \pm 0 |
| Hindlimb muscle | 0 \pm 0 | 0 \pm 0 | 0 \pm 0 | 13 \pm 7 | 88 \pm 6 |
| Spleen | 98 \pm 4 | 84 \pm 6 | 13 \pm 10 | 84 \pm 6 | 11 \pm 6 |
| Lung | 1 \pm 2 | 1 \pm 1 | 1 \pm 2 | 1 \pm 2 | 1 \pm 1 |
| Liver | 1 \pm 2 | 1 \pm 1 | 1 \pm 1 | 1 \pm 2 | 1 \pm 1 |
| Brain | 0 \pm 0 | 0 \pm 0 | 0 \pm 0 | 0 \pm 0 | 0 \pm 0 |
| Kidney | 0 \pm 0 | 0 \pm 0 | 0 \pm 0 | 0 \pm 0 | 0 \pm 0 |
| Intestine | 0 \pm 0 | 0 \pm 0 | 0 \pm 0 | 0 \pm 0 | 0 \pm 0 |

Each value shows a distribution ratio (%) into organs of transfected macrophages/monocytes (mean \pm SD). *i.v.* intravenous injection into the vein; *i.m.* direct injection into the jeopardized muscle

ischemic/non-ischemic myocardium) compared with the other three treatments ($P < 0.05$, ANOVA), that is, intravenous administration of saline ($35 \pm 10\%$, $n = 8$), intramuscular administration of naked DNA encoding FGF4 ($50 \mu\text{g}$, direct intramyocardial injection after thoracotomy) ($58 \pm 5.3\%$, $n = 8$), and intravenous administration of the same number of non-transfected macrophages ($42 \pm 12\%$, $n = 8$) (Fig. 4A). Histological analyses revealed angiogenesis in the ischemic tissue after the administration of transfected cells (Figs. 4B and C). Similar results were observed in the mouse model with hindlimb ischemia. Intravenous injection of FGF4-gene-transfected monocytes (1.0×10^6) enhanced regional blood flow in the ischemic leg (Fig. 4D). The increase of blood flow in the mice with transfected monocytes ($93 \pm 22\%$ in terms of flow ratio of ischemic/non-ischemic leg) was significantly larger than those obtained with the other three treatments described above (38 ± 12 , 55 ± 12 , and $39 \pm 15\%$, $P < 0.05$, ANOVA). Neither lymph node swelling in any part of the body nor pathologic change in the spleen or lung, such as angioma or abnormal immune response, was found in any of the animals.

Discussion

The advantages of the present method are as follows. First, genes can easily be transfected into phagocytes (macrophages/monocytes). In preliminary experiments, we found that genes can also be transfected into endothelial progenitor cells [25]. Compared with other transfection method, the transfection efficiency was high ($68 \pm 11\%$) and it is not necessary to use a potentially hazardous viral vector [2, 26, 32]. Second, the phagocytes can target the pathologic tissues by chemotaxis even after intravenous injection, and higher tar-

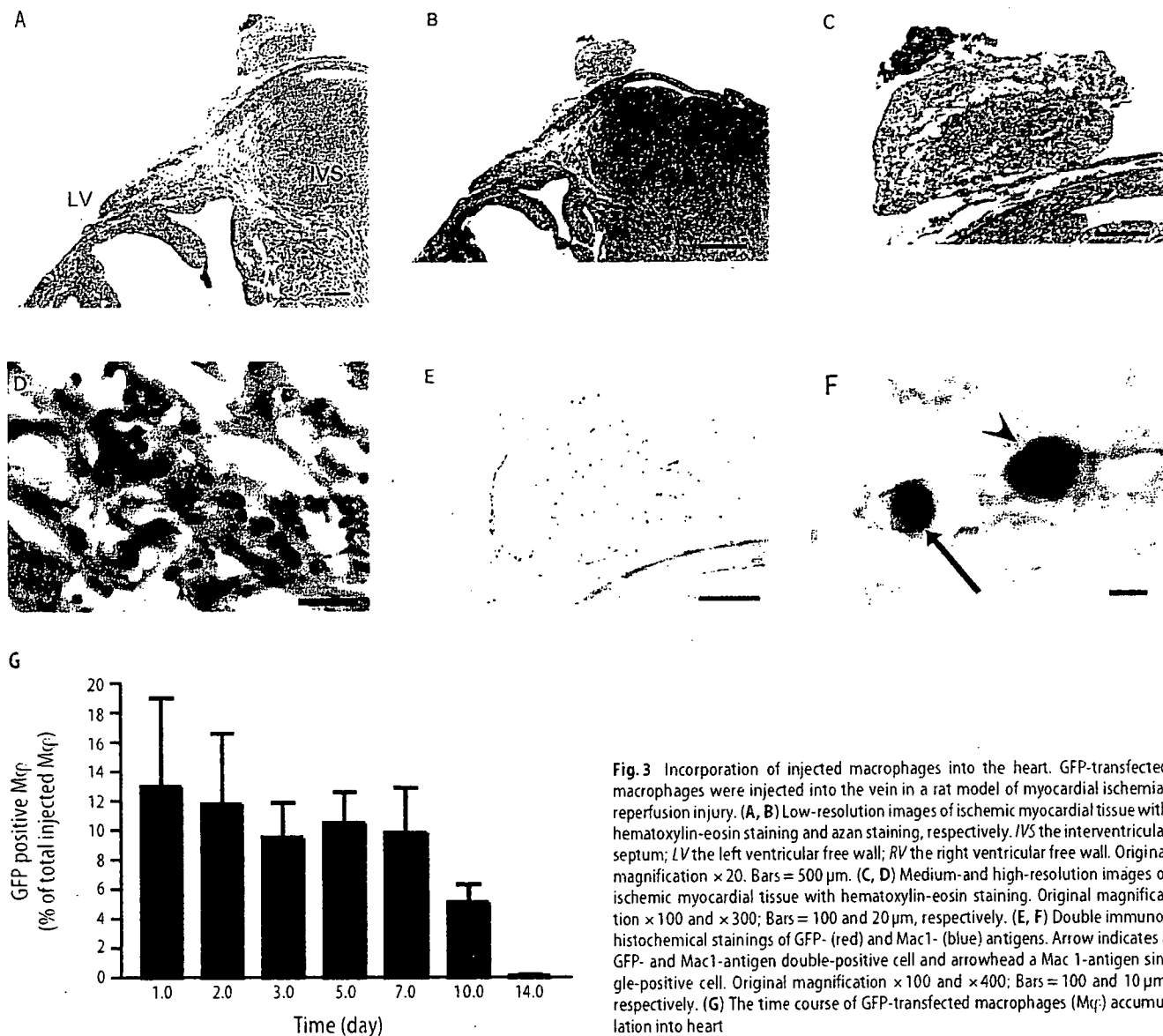


Fig. 3 Incorporation of injected macrophages into the heart. GFP-transfected macrophages were injected into the vein in a rat model of myocardial ischemia-reperfusion injury. (A, B) Low-resolution images of ischemic myocardial tissue with hematoxylin-eosin staining and azan staining, respectively. *IVS* the interventricular septum; *LV* the left ventricular free wall; *RV* the right ventricular free wall. Original magnification $\times 20$. Bars = 500 μm . (C, D) Medium- and high-resolution images of ischemic myocardial tissue with hematoxylin-eosin staining. Original magnification $\times 100$ and $\times 300$; Bars = 100 and 20 μm , respectively. (E, F) Double immunohistochemical stainings of GFP- (red) and Mac1- (blue) antigens. Arrow indicates a GFP- and Mac1-antigen double-positive cell and arrowhead a Mac 1-antigen single-positive cell. Original magnification $\times 100$ and $\times 400$; Bars = 100 and 10 μm , respectively. (G) The time course of GFP-transfected macrophages (Mφ) accumulation into heart

getting is available if they are administered locally. The injection is repeatable. We confirmed that the angiogenic gene-transfected phagocytes enhanced angiogenesis after ischemia-reperfusion injury in rat heart and ameliorated ischemia in a mouse hindlimb model.

The injected phagocytes migrated into pathologic tissues, presumably in response to the release of cytokines such as monocyte chemoattractant protein 1 by injured endothelial cells [27]. Adhesion molecules such as P-selectin [28] are probably involved in the recruitment of phagocytes to the vessel wall. The injected phagocytes also migrated to the spleen, but no pathologic change was found in the spleen.

The present method has several advantages over conventional methods of cell-based gene therapy such as fi-

broblast-based and smooth muscle cell-based approaches [18, 19, 33, 34]. For example, monocytes do not aggregate in vessels, while fibroblasts or smooth muscle cells cannot be injected intravenously because of aggregation. The transfected phagocytes not only synthesize protein from the transfected gene, but also are partially targeted to the impaired tissue. In addition, the transfection rate was better than those of methods such as lipofection, viral vectors and electroporation [26, 29]. The newly developed technique of nucleofection has a transfection efficiency of 40–70% [30], which is similar to that of our method, but our procedure is easier to use [30, 31]. Further, the therapeutic effect obtained here was superior to that of conventional gene therapy which we reported previously, i.e., intramuscular injection of

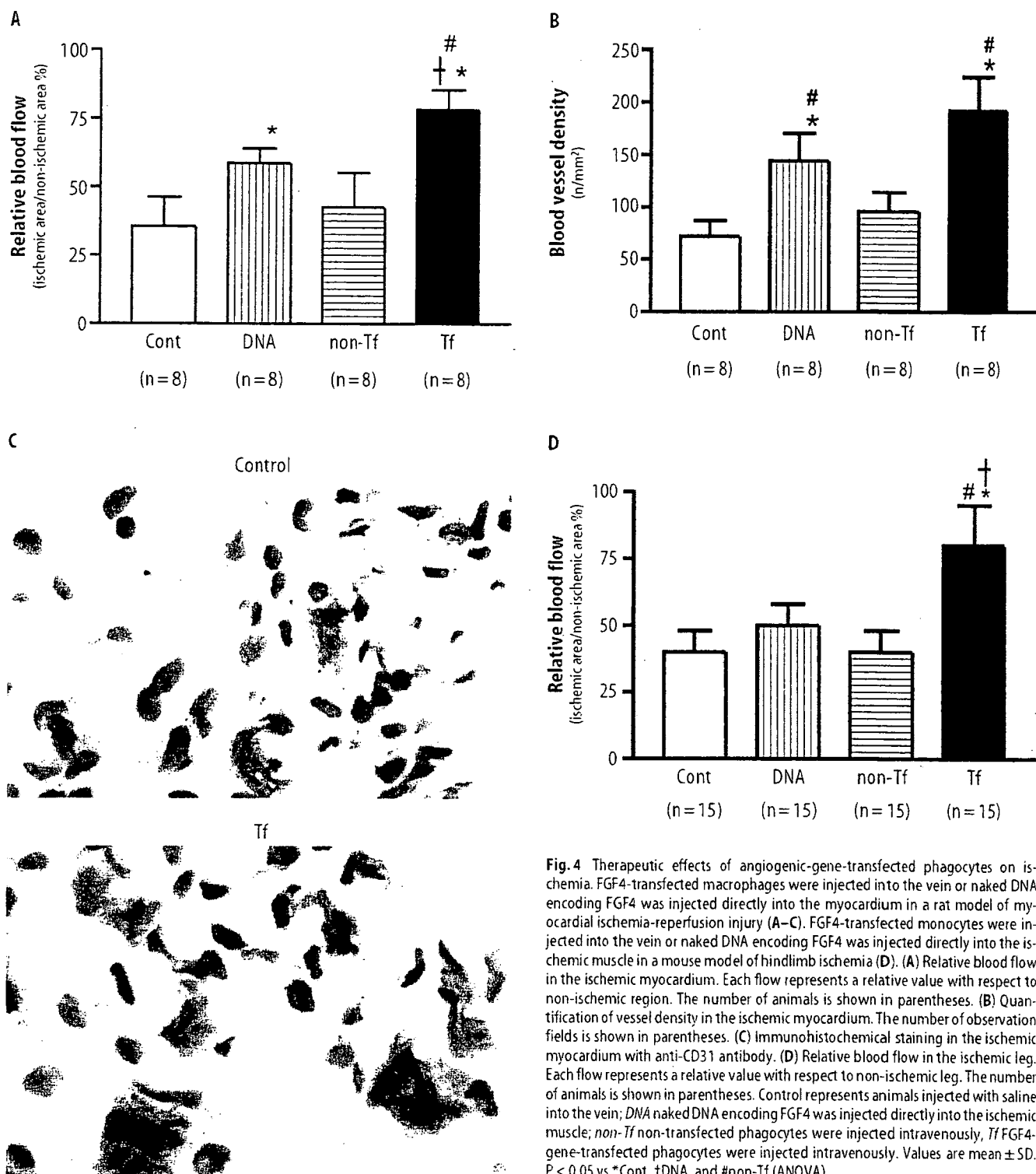


Fig. 4 Therapeutic effects of angiogenic-gene-transfected phagocytes on ischemia. FGF4-transfected macrophages were injected into the vein or naked DNA encoding FGF4 was injected directly into the myocardium in a rat model of myocardial ischemia-reperfusion injury (A–C). FGF4-transfected monocytes were injected into the vein or naked DNA encoding FGF4 was injected directly into the ischemic muscle in a mouse model of hindlimb ischemia (D). (A) Relative blood flow in the ischemic myocardium. Each flow represents a relative value with respect to non-ischemic region. The number of animals is shown in parentheses. (B) Quantification of vessel density in the ischemic myocardium. The number of observation fields is shown in parentheses. (C) Immunohistochemical staining in the ischemic myocardium with anti-CD31 antibody. (D) Relative blood flow in the ischemic leg. Each flow represents a relative value with respect to non-ischemic leg. The number of animals is shown in parentheses. Control represents animals injected with saline into the vein; *DNA* naked DNA encoding FGF4 was injected directly into the ischemic muscle; *non-Tf* non-transfected phagocytes were injected intravenously, *Tf* FGF4-gene-transfected phagocytes were injected intravenously. Values are mean \pm SD. $P < 0.05$ vs *Cont, †DNA, and #non-Tf (ANOVA)

naked DNA, in ischemia models of heart and leg [17]. The major disadvantage of our method is the cell preparation time of 2 weeks before therapy can be started, and further work is needed to speed up this process.

Acknowledgements The authors wish to thank Jobu Itoh, Yoshiko Shinozaki, and Takayuki Hasegawa for their technical work.

References

- Pfeifer A, Verma IM (2001) Gene therapy: promises and problems. *Annu Rev Genomics Hum Genet* 2:177-211
- Watson DJ, Kobinger GP, Passini MA, Wilson JM, Wolfe JH (2002) Targeted transduction patterns in the mouse brain by lentivirus vectors pseudotyped with VSV, Ebola, Mokola, LCMV, or MuLV envelope proteins. *Mol Ther* 5:528-537
- Li Q, Bolli R, Qiu Y, Tang XL, Guo Y, French BA (2001) Gene therapy with extracellular superoxide dismutase protects conscious rabbits against myocardial infarction. *Circulation* 103:1893-1898
- Ferber D (2001) Gene therapy. Safer and virus-free? *Science* 294:1638-1642
- Kay MA, Glorioso JC, Naldini L (2001) Viral vectors for gene therapy: the art of turning infectious agents into vehicles of therapeutics. *Nat Med* 7:33-40
- Isner JM (2002) Myocardial gene therapy. *Nature* 415:234-239
- Nishikawa M, Hashida M (2002) Nonviral approaches satisfying various requirements for effective in vivo gene therapy. *Biol Pharm Bull* 25:275-283
- Schakowski F, Buttgereit P, Mazur M, Mazur M, Marten A, Schottker B, Gorschluter M, Schmidt-Wolf IG (2004) Novel non-viral method for transfection of primary leukemia cells and cell lines. *Genet Vaccines Ther* 2:1
- Tomasoni S, Benigni A (2004) Gene therapy: how to target the kidney. Promises and pitfalls. *Curr Gene Ther* 4:115-122
- Losordo DW, Vale PR, Symes JF, Dunnington CH, Esakof DD, Maysky M, Ashare AB, Lathi K, Isner JM (1998) Gene therapy for myocardial angiogenesis: initial clinical results with direct myocardial injection of phVEGF165 as sole therapy for myocardial ischemia. *Circulation* 98:2800-2804
- Kornowski R, Leon MB, Fuchs S, Vodovotz Y, Flynn MA, Gordon DA, Pierre A, Kovacs I, Keiser JA, Epstein SE (2000) Electromagnetic guidance for catheter-based transendocardial injection: a platform for intramyocardial angiogenesis therapy. Results in normal and ischemic porcine models. *J Am Coll Cardiol* 35:1031-1039
- Laitinen M, Hartikainen J, Hiltunen MO, Eränen J, Kiviniemi M, Narvanen O, Makinen K, Manninen H, Syvanne M, Martin JF, Laakso M, Yla-Herttuala S (2000) Catheter-mediated vascular endothelial growth factor gene transfer to human coronary arteries after angioplasty. *Hum Gene Ther* 11:263-270
- Ramsay SC, Weiller C, Myers R, Cremer JE, Luthra SK, Lammertsma AA, Frackowiak RS (1992) Monitoring by PET of macrophage accumulation in brain after ischaemic stroke. *Lancet* 339:1054-1055
- Tabata Y, Ikada Y (1987) Macrophage activation through phagocytosis of muramyl dipeptide encapsulated in gelatin microspheres. *J Pharm Pharmacol* 39:698-704
- Tabata Y, Ikada Y (1988) Macrophage phagocytosis of biodegradable microspheres composed of L-lactic acid/glycolic acid homo- and copolymers. *J Biomed Mater Res* 22:837-858
- Ikada Y, Tabata Y (1998) Protein release from gelatin matrices. *Adv Drug Deliv Rev* 31:287-301
- Kasahara H, Tanaka E, Fukuyama N, Sato E, Sakamoto H, Tabata Y, Ando K, Iseki H, Shinozaki Y, Kimura K, Kuwabara E, Koide S, Nakazawa H, Mori H (2003) Biodegradable gelatin hydrogel potentiates the angiogenic effect of fibroblast growth factor 4 plasmid in rabbit hindlimb ischemia. *J Am Coll Cardiol* 41:1056-1062
- Xie Y, Yang ST, Kniss DA (2001) Three-dimensional cell-scaffold constructs promote efficient gene transfection: implications for cell-based gene therapy. *Tissue Eng* 7:585-598
- Panetta CJ, Miyauchi K, Berry D, Sunari RD, Holmes DR, Schwartz RS, Caplice NM (2002) A tissue-engineered stent for cell-based vascular gene transfer. *Hum Gene Ther* 13:433-441
- Gidh-Jain M, Huang B, Jain P, el-Sherif N (1996) Differential expression of voltage-gated K⁺ channel genes in left ventricular remodeled myocardium after experimental myocardial infarction. *Circ Res* 79:669-675
- Takeshita S, Zheng LP, Brogi E, Kearney M, Pu LQ, Bunting S, Ferrara N, Symes JF, Isner JM (1994) Therapeutic angiogenesis. A single intraarterial bolus of vascular endothelial growth factor augments revascularization in a rabbit ischemic hind limb model. *J Clin Invest* 93:662-670
- Ribeiro RA, Flores CA, Cunha FQ, Ferreira SH (1991) IL-8 causes in vivo neutrophil migration by a cell-dependent mechanism. *Immunology* 73:472-477
- Fukuyama N, Ichimori K, Su Z, Ishida H, Nakazawa H (1996) Peroxynitrite formation from activated human leukocytes. *Biochem Biophys Res Commun* 224:414-419
- Mori H, Haruyama S, Shinozaki Y, Okino H, Iida A, Takanashi R, Sakuma I, Hussein WK, Payne BD, Hoffman JI (1992) New nonradioactive microspheres and more sensitive X-ray fluorescence to measure regional blood flow. *Am J Physiol* 263:H1946-H1957
- Nagaya N, Kangawa K, Kanda M, Uematsu M, Horio T, Fukuyama N, Hino J, Harada-Shiba M, Okumura H, Tabata Y, Mochizuki N, Chiba Y, Nishioka K, Miyatake K, Asahara T, Hara H, Mori H (2003) Hybrid cell-gene therapy for pulmonary hypertension based on phagocytosing action of endothelial progenitor cells. *Circulation* 108:889-895
- Kobinger GP, Deng S, Louboutin JP, Vatamaniuk M, Matschinsky F, Markmann JF, Raper SE, Wilson JM (2004) Transduction of human islets with pseudotyped lentiviral vectors. *Hum Gene Ther* 15:211-219
- Leonard EJ, Yoshimura T (1990) Human monocyte chemoattractant protein-1 (MCP-1). *Immunol Today* 11:97-101
- Ikeda Y, Young LH, Lefer AM (2002) Attenuation of neutrophil-mediated myocardial ischemia-reperfusion injury by a calpain inhibitor. *Am J Physiol Heart Circ Physiol* 282:H1421-H1426
- Veit K, Boissel JP, Buerke M, Grosser T, Meyer J, Darius H (1999) Highly efficient liposome-mediated gene transfer of inducible nitric oxide synthase in vivo and in vitro in vascular smooth muscle cells. *Cardiovasc Res* 43:808-822
- Maasho K, Marusina A, Reynolds NM, Coligan JE, Borrego F (2004) Efficient gene transfer into the human natural killer cell line, NKL, using the Amaxa nucleofection system. *J Immunol Methods* 284:133-140
- Mertz KD, Weisheit G, Schilling K, Luers GH (2002) Electroporation of primary neural cultures: a simple method for directed gene transfer in vitro. *Histochem Cell Biol* 118:501-506
- Lei Y, Haider HK, Shujia J, Sim ES (2004) Therapeutic angiogenesis: Devising new strategies based on past experiences. *Basic Res Cardiol* 99:121-132
- Ott HC, McCue J, Taylor DA (2005) Cell-based cardiovascular repair: The hurdles and the opportunities. *Basic Res Cardiol* 100:504-517
- Koch KC, Schaefer WM, Liehn EA, Rammos C, Mueller D, Schroeder J, Dimassi T, Stopinski T, Weber C (2006) Effect of catheter-based transendocardial delivery of stromal cell-derived factor 1 α on left ventricular function and perfusion in a porcine model of myocardial infarction. *Basic Res Cardiol* 101:69-77

Crystal structures of catrocollastatin/VAP2B reveal a dynamic, modular architecture of ADAM/adamalysin/reprolysin family proteins

Tomoko Igarashi^a, Satohiko Araki^b, Hidezo Mori^a, Soichi Takeda^{a,*}

^a Department of Cardiac Physiology, National Cardiovascular Center Research Institute 5-7-1 Fujishiro-dai, Suita, Osaka 565-8565, Japan

^b Sugashima Marine Biological Laboratory, Graduate School of Science, Nagoya University, Toba, Mie 517-0004, Japan

Received 26 January 2007; revised 29 March 2007; accepted 20 April 2007

Available online 30 April 2007

Edited by Christian Griesinger

Abstract Catrocollastatin/vascular apoptosis-inducing protein (VAP)2B is a metalloproteinase from *Crotalus atrox* venom, possessing metalloproteinase/disintegrin/cysteine-rich (MDC) domains that bear the typical domain architecture of a disintegrin and metalloproteinase (ADAM)/adamalysin/reprolysin family proteins. Here we describe crystal structures of catrocollastatin/VAP2B in three different crystal forms, representing the first reported crystal structures of a member of the monomeric class of this family of proteins. The overall structures show good agreement with both monomers of atypical homodimeric VAP1. Comparison of the six catrocollastatin/VAP2B monomer structures and the structures of VAP1 reveals a dynamic, modular architecture that may be important for the functions of ADAM/adamalysin/reprolysin family proteins.

© 2007 Federation of European Biochemical Societies. Published by Elsevier B.V. All rights reserved.

Keywords: ADAM; Adamalysin; Reprolysin; MDC protein; Metalloproteinase disintegrin; Apoptotic toxin

1. Introduction

Hemorrhagic snake venoms induce local and systemic hemorrhaging by disrupting the walls of the blood vessels in envenomed patients [1]. In vitro, they induce apoptosis specifically in cultured vascular endothelial cells [2]. Vascular apoptosis-inducing protein (VAP)1 and VAP2 were originally isolated from *Crotalus atrox* venom [3,4], and similar apoptotic toxins have been isolated from other snake venoms [5–7]. VAP1 is a disulfide-bridged homodimeric protein with an apparent molecular weight of 110 kDa, and an isoelectric point of 8.5. VAP2 is a single chain protein with a MW of 55 kDa and an isoelectric point of 4.5 [3,4,8]. VAPs are members of the P-III class of snake venom metalloproteinases (SVMPs), possessing a metalloproteinase/disintegrin/cysteine-rich (MDC) domain architecture typical of a disintegrin and metalloproteinase (ADAM)/adamalysin/reprolysin family proteins [9,10]. VAP-induced apoptosis is dependent on its catalytic activity [8], is

inhibited by antibodies to integrins $\alpha 3$, $\alpha 6$, $\beta 1$ and CD9 [11], and involves activation of specific caspases [12]. However, the physiological targets of VAPs and the underlying mechanism of VAP-induced apoptosis remain elusive.

ADAMs are a family of mammalian membrane-anchored glycoproteins that have been implicated in the processing of cell surface and extracellular matrix proteins [13,14]. The crystal structures of several P-I class SVMPs, which contain only a metalloproteinase (M)-domain, and the isolated M and disintegrin/cysteine-rich (DC) domains of ADAMs have been determined [15–18]. However, structures of ADAM/adamalysin/reprolysin family proteins that include the entire MDC domain have not been determined. The relevance of the multidomain structure to the catalytic and adhesive functions of this family of proteins is an important issue that remains to be elucidated. To better understand the structure–function relationship of ADAM/adamalysin/reprolysin family proteins, and how it relates to the molecular mechanism of VAP-induced apoptosis, we have been engaged in crystallographic studies of VAPs. Recently, we determined the crystal structure of VAP1, revealing the MDC domain architecture for the first time [19]. Although the intrinsic two-fold symmetry of atypical homodimeric VAP1 conferred a great advantage for both its crystallization and structural resolution, the possibility remained that the spatial arrangement of the MDC domains of VAP1 differed from that of monomeric SVMPs and ADAMs, due to crystallographic restraints imposed on the molecule. The majority of ADAMs and SVMPs do not form VAP1-type dimers, most likely due to the lack of a consensus QDHSK sequence [19] (residues 320–324 in VAP1, in which the N ζ atom of Lys324 is coordinated by the six oxygen atoms of another monomer and plays a pivotal role in dimer formation), and Cys365, which are conserved among the dimeric SVMPs (Supplementary Fig. 1). Therefore, to elucidate the general architecture of proteins of the ADAM/adamalysin/reprolysin family, we crystallized VAP2 and determined its structure. We modeled all of the structures as monomers of VAP2B, which is identical to catrocollastatin, a protein previously isolated as a platelet aggregation inhibitor [20]. Here we describe the structure of catrocollastatin/VAP2B, as determined in three different crystal forms. These are the first reported crystal structures of the monomeric class of proteins in ADAM/adamalysin/reprolysin family.

2. Materials and methods

Protein preparation and crystallization were performed as previously described [21]. The diffraction data sets were collected at the

*Corresponding author. Fax: +81 6 6872 7485.

E-mail address: stakeda@ri.ncvc.go.jp (S. Takeda).

Abbreviations: ADAM, a disintegrin and metalloproteinase; MDC, Metalloproteinase/disintegrin/cysteine-rich; SVMP, Snake venom metalloproteinase; HVR, Hyper-variable-region; ncs, Non-crystallographic symmetry; VAP, Vascular apoptosis-inducing protein; PEG, Polyethyleneglycol

SPring-8 beamline BL41XU using the ADSC quantum 315 CCD detector with a wavelength of 1.0 Å at 100 K. Images were reduced using HKL2000 [22] (Table 1). Structures were solved using the molecular replacement (MR) method and the MOLREP program of the CCP4 suite [23], with the structure of VAP1 (2ERO) as a starting model. The M- and C-domains of the VAP1 were used separately as the search models. An MR solution was initially obtained from the Form 2-2 crystal data set, which assumed two M-domains and two C-domains in the asymmetric units. After the model was manually rebuilt using TURBO-FRODO [24], it was subjected to torsional molecular dynamic refinements using CNS [25]. Iterative refinements and manual rebuilding of the model improved the electron-density map and enabled us to model the remaining part of the molecule. The composite omit electron-density maps created by CNS were used to confirm the chain tracing. After the polypeptide chains were modeled, we modeled zinc and calcium ions and the inhibitor GM6001 (3-(*N*-hydroxycarbonyl)-2-isobutyl-propanoyl-Trp-methylamide), then the components of the carbohydrate chain linked to Asn371.

The two monoclinic crystal structures were solved by MR with the domains of the refined Form 2-2 crystal structure as a starting model. In all three crystal forms, the asymmetric unit contained two monomers of catrocollastatin/VAP2B. Refinement statistics are shown in Table 1. During the course of our analysis, we found a point mutation (F203V) in the crystallized specimens. By comparing the structures with that of VAP1, which has a phenylalanine at this position, we determined that this mutation does not introduce a large structural

change or affect the flexibility of the molecule. Graphical representations were prepared using the programs TURBO-FRODO [24], MOLSCRIPT [26], RASTER3D [27] and PyMOL [28].

3. Results and discussion

3.1. Structural determination

Purified VAP2 was crystallized in variety of forms [21]. In the current study, we determined the structures of three of these crystal forms. Previously, we observed that the VAP2 preparation is a mixture of two homologous polypeptide chains, VAP2A and VAP2B [29]. To identify the molecules in the crystals as either VAP2A or catrocollastatin/VAP2B, we carefully analyzed the composite omit electron-density maps corresponding to the 11 amino acid residues that are distinct between the two proteins (Supplementary Fig. 1). Based on this assessment, the major component in the three crystals was determined to be catrocollastatin/VAP2B. Therefore, in the present study, we modeled all six molecules as catrocollastatin/VAP2B. The indole ring of GM6001 provided additional

Table 1
Data collection and refinement statistics

| | Form 2-1 | Form 2-2 | Form 2-5 |
|--|--------------------|--------------------|--------------------|
| <i>Data collection</i> | | | |
| Space group | $P2_1$ | $P2_12_12_1$ | $C2$ |
| Cell dimensions | | | |
| <i>a</i> , <i>b</i> , <i>c</i> (Å) | 56.9, 138.0, 59.2 | 57.7, 118.2, 138.5 | 220.7, 79.5, 58.7 |
| α , β , γ (°) | 90, 91.5, 90 | 90, 90, 90 | 90, 91.7, 90 |
| Resolution (Å) (high resolution shell) | 50–2.15(2.23–2.15) | 50–2.50(2.59–2.50) | 50–2.70(2.80–2.70) |
| No. of unique reflections | 48664(4428) | 33288(2925) | 26911(2313) |
| ^a <i>R</i> _{merge} | 0.081(0.196) | 0.089(0.321) | 0.085(0.231) |
| <i>I</i> /σ(<i>I</i>) | 9.8(4.6) | 10.3(3.7) | 10.1(5.5) |
| Completeness (%) | 98.1(89.5) | 98.6(88.4) | 95.9(82.5) |
| Redundancy | 3.3(2.0) | 6.5(3.3) | 3.4(2.8) |
| <i>Refinement</i> | | | |
| Resolution (Å) (high resolution shell) | 50–2.15(2.23–2.15) | 50–2.50(2.59–2.50) | 50–2.70(2.80–2.70) |
| No. of reflections | 48628(4386) | 33099(2922) | 26907(2276) |
| ^b <i>R</i> _{work} | 0.175(0.195) | 0.227(0.316) | 0.199(0.264) |
| ^c <i>R</i> _{free} | 0.228(0.277) | 0.286(0.399) | 0.260(0.328) |
| Average B-factors (No. of atoms) | | | |
| All atoms | 19.9(7292) | 38.5(6801) | 25.1(6823) |
| Protein | 18.5(6422) | 38.1(6438) | 24.7(6438) |
| Main chain atoms | 17.2 | 36.9 | 23.1 |
| Side chain atoms | 19.9 | 39.5 | 26.5 |
| Zn ²⁺ | 13.6(2) | 24.9(2) | 18.7(2) |
| Ca ²⁺ | 14.6(6) | 41.4(6) | 21.5(6) |
| Carbohydrate | 54.2(139) | 81.4(88) | 37.4(226) |
| GM6001 | 16.2(56) | 36.9(56) | 0(-) |
| Water | 26.5(668) | 31.6(211) | 22.2(151) |
| R.m.s deviations | | | |
| Bond lengths (Å) | 0.0047 | 0.0065 | 0.0045 |
| Bond angles (°) | 1.20 | 1.44 | 1.14 |
| Ramachandran plot | | | |
| Most favored | 87.2% | 84.3% | 82.8% |
| Additional allowed | 12.1% | 15.0% | 16.4% |
| Generously allowed | 0.4% | 0.6% | 0.4% |
| Disallowed | 0.1%(R297B) | 0.1%(R297B) | 0.3%(R297A/R297B) |

^a*R*_{merge} = $\sum_i |I_i(hkl) - \langle I(hkl) \rangle| / \sum_i I_i(hkl)$, where $I_i(hkl)$ is the *i*th intensity measurement of reflection *hkl* and $\langle I(hkl) \rangle$ is its average.

^b*R*_{work} = $\sum_i |F_{obs} - F_{calc}| / \sum_i |F_{obs}|$.

^c*R*_{free} = *R*-value for a randomly selected subset (5%) of the data that were not used for minimization of the crystallographic residual. A single crystal was used for measurement of each data set.

crystal contacts for the neighboring molecule, resulting in crystals that were distinct from the inhibitor-free form.

3.2. Overall structure

The overall structure of catrocollastatin/VAP2B is presented in Fig. 1. The structure of the M-domain was very similar to the corresponding structures in adamalysin II [15] and ADAM33 [17], with a flat elliptical shape and a core formed by a five-stranded β -sheet and four α -helices. A conserved methionine (Met357, Met-turn) was present downstream of the consensus HEXXHXXGXXHD sequence, which contains three histidines (His333, His337 and His343) that function as ligands of the catalytic zinc atom, and a glutamate residue (Glu334) that functions as the general base (Fig. 2). These structural features are typical of the metzincine family of metalloproteinases [30,31]. A bound calcium ion was identified opposite the active site cleft and close to the crossover point of

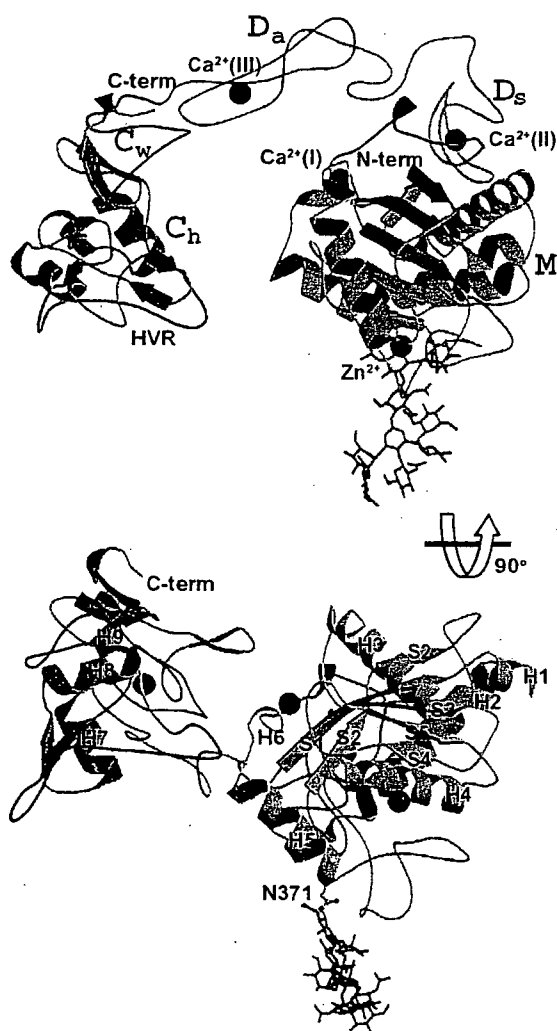


Fig. 1. Ribbon diagrams of catrocollastatin/VAP2B. The M-domain, linker, D_s , D_a , C_w , and C_h segments and the HVRs are shown in red, yellow, grey, cyan, pink, grey, green and blue, respectively. Zinc and calcium ions are represented as red and black spheres, respectively. The carbohydrate moiety linked to Asn371 is shown as a stick representation.

the N- and C-terminal segments of the M-domain (Ca^{2+} -binding site I), as in the structures of adamalysin II [15] and ADAM33 [17]. The M-domain is followed by the D-domain, which can be sub-divided into “shoulder” (D_s) and “arm” (D_a) segments. D_s protrudes from the M-domain close to Ca^{2+} -binding site I, opposing the catalytic zinc atom. The C-domain is sub-divided into “wrist” (C_w) and “hand” (C_h) segments. Because of its curved structure, with the concave surface toward the M-domain, the distal portion of C_h comes close to and faces the catalytic site, thus the entire molecule adopts a C-shaped conformation. In the D_s and D_a segments, there are Ca^{2+} ions (sites II and III, respectively) that stabilize the structure. Details of the Ca^{2+} -coordinations are shown in Supplementary Fig. 2. The distal portion of the C-shape, spanning residues 561–582 of the C_h domain, is the region in which the amino acid sequence is most divergent and variable in length among ADAM/adamalysin/reprolysin family proteins (Fig. 2 and Supplementary Fig. 1). We designated this region as the hyper-variable-region (HVR), and have proposed that it represents a potential exosite for target recognition [19]. Aside from Cys377, whose side chain is embedded in the hydrophobic core, all 34 cysteinyl residues are involved in disulfide bonding. The number and spacing of cysteinyl residues, and the structures of the Ca^{2+} -binding sites are strictly conserved among ADAM/adamalysin/reprolysin family proteins (Fig. 2 and Supplementary Fig. 1). Fig. 2 shows the sequence alignment of a selected subset of ADAMs and SVMs; alignment of the full sequences of catrocollastatin/VAP2B and 107 proteins of the ADAM/adamalysin/reprolysin family can be found in Supplementary Fig. 1.

3.3. Flexible modular architecture

The structures of the M-domain (Fig. 3A), D_s (Fig. 3C), and C_w/C_h (Fig. 3B) of the six catrocollastatin/VAP2B molecules were nearly identical (r.m.s.d of 0.33, 0.45 and 0.59 Å, respectively). They were also essentially the same as the corresponding regions of VAP1 (r.m.s.d of 0.78, 0.63 and 1.1 Å, respectively (Fig. 3A–C)). However, the relative orientations of the sub-domains were quite variable. The largest difference was observed when the M domains of the six catrocollastatin/VAP2B molecules are superimposed. The $D_s/D_a/C_w/C_h$ portion should be rotated by approximately 13° relative to the M-domain, bringing about a 15-Å displacement at the distal end of C_h (Fig. 3A). A similar plot of the C_h segments superimposed shows less hinge bending, bringing approximately a 6-Å displacement at the distal portion of D_s (Fig. 3B). This conformed that the hinge motion occurs largely between the M domain and D_s . The bending of the main chain at two residues, Val403 and Gly438, is most prominent (Fig. 3C), however, the entire linker region (which is defined by the segment between two structural Ca^{2+} -binding sites, I and II) also moves in concert with the bending motion of Val403 (Fig. 3D). In this concerted movement of the linker, the side chain of Leu408 in D_s is positioned at a pivotal point (Fig. 3D and E). The main chain carbonyl oxygen atom of Leu408 coordinates the calcium ion at site II, whereas, the side-chain of Leu408 protrudes from D_s and interacts with a small hydrophobic cavity on the surface of the M domain (Fig. 3D). A bulky hydrophobic residue (Leu or Phe or Tyr) at this position is highly conserved among ADAM/adamalysin/reprolysin family proteins (Supplementary Fig. 1), and its side chain probably functions as

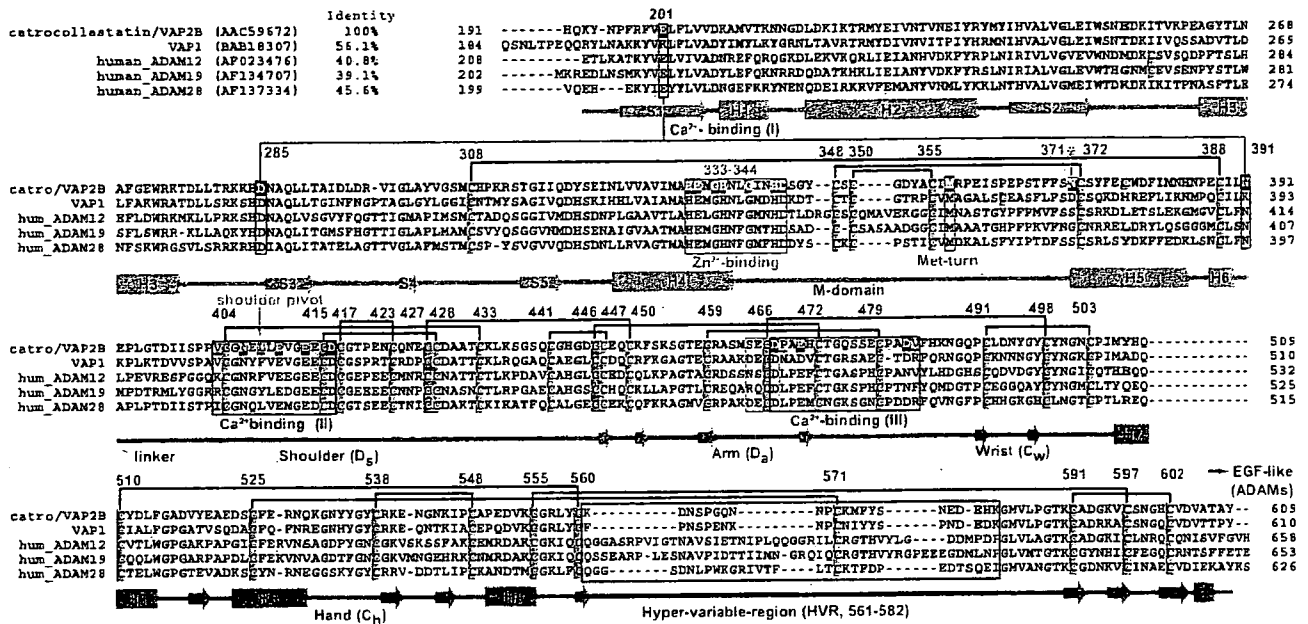


Fig. 2. Sequence alignment of catrocollastatin/VAP2B, VAP1 and human ADAMs. The cysteinyl residues and the conserved residues are shaded in pink and yellow, respectively. Disulfide bridges, secondary structures and domains are drawn schematically. The HVR, Ca²⁺-binding sites, Zn²⁺-binding site and disintegrin-loop are boxed in blue, red, green and cyan, respectively. The Ca²⁺-coordinating residues are shaded in red.

a universal joint (shoulder joint) that allows D_s to adopt various orientations with respect to the M domain. The linker has fewer specific interactions with D_s and has a rather high B-factor (Supplementary Figs. 3 and 4). It is divergent and variable in length (7–12 aa), particularly in human ADAMs (Supplementary Fig. 1), thus may function primarily in connecting D_s to the M domain. The linker may also restrict the mobility of the shoulder joint, and thus determine the preferred orientation of the M domain of each ADAMs relative to the rest of the molecule for distinct targets. The residues forming the hydrophobic cavity with which Leu408 interacts are less conserved and also have relatively high B-factors (Supplementary Figs. 3 and 4). Thus they may also contribute to the flexibility of the shoulder joint.

Previously, we suggested a putative mechanism of HVR-mediated target recognition and catalysis by this family of proteins [19]. The present study allows us to incorporate into the previous model that intrinsic flexibility may be important for fine-tuning substrate recognition, by adjusting the spatial alignment of the catalytic and adhesion sites during the catalytic cycle (Fig. 3F). The structure of the lower half of the D_a segment in catrocollastatin/VAP2B was different from that of VAP1 (Fig. 3B and Supplementary Fig. 3C), most likely due to the substitution of Glu470 (in catrocollastatin/VAP2B) with Asp471 (in VAP1), and the insertion of Pro480 (in catrocollastatin/VAP2B). All the ADAMs, with the exception of ADAMs 10 and 17, which lack Ca²⁺-binding site III, and the monomeric P-III and P-IV SVMPs contain Glu470 and Pro480 (see Supplementary Fig. 1). Thus, it is likely that they adopt a more catrocollastatin/VAP2B-like structure. As was observed in VAP1, the disintegrin-loop is packed by C_w, and forms a less flexible D_a/C_w junction, and therefore is unavailable for ligand binding. Differences in the orientation of D_a and C_w among these proteins may be important for proper spatial alignment of the catalytic and adhesion units and for substrate binding specificity. The angle between C_w and C_h

in catrocollastatin/VAP2B was nearly invariant. It was essentially the same as that seen in VAP1 (Fig. 3B), but substantially different than that of ADAM10 [18,19]. Whether different ADAM/adamalsin/reprolysin family proteins have distinct C_w/C_h orientations remains to be established.

3.4. Modular architecture and post-translational processing

The disintegrins that are commonly found in Viperid venoms are typically generated by proteolytic processing of larger precursor molecules, the P-II class of SVMPs, which contain an M-domain plus a disintegrin portion [32,33]. The flexible modular structure described above points to a potential mechanism of selection of cleavage sites for this processing event. The cleavage sites of the medium-sized disintegrins (~70 amino acids) are usually within Ca²⁺-binding site II, whereas, those of the shorter ones (41–51 residues) are at the boundary between D_s and D_a. The longer disintegrins (~84 residues) are processed within the linker between M and D_s (Fig. 4 and Supplementary Fig. 1). Most of the P-II SVMPs have fewer cysteine residues within their D_s segment (3 or 5 cysteine residues, see Supplementary Fig. 1) compared to P-III SVMPs, and thus have fewer disulfide bonds. Additionally, they contain substitutions of the calcium-binding residues at site II, indicating that they have a less stable D_s structure compared to P-III SVMPs. Long disintegrins have the same number of cysteine residues (7 cysteine residues) and Ca²⁺-binding residues at site II as P-III SVMPs and ADAMs, and thus would be predicted to have a more stable D_s structure, which may account for their cleavage at the linker between M and D_s. A protective role for calcium against auto proteolysis in the linker region has been reported [34], and the linker region is usually removed from P-I SVMPs post-translationally [35]. Collectively, these observations suggest that differential susceptibility to proteolysis in the linker region and D_s, due to variability in the number of disulfide bonds and the presence or absence of bound calcium at site II, may underlie the

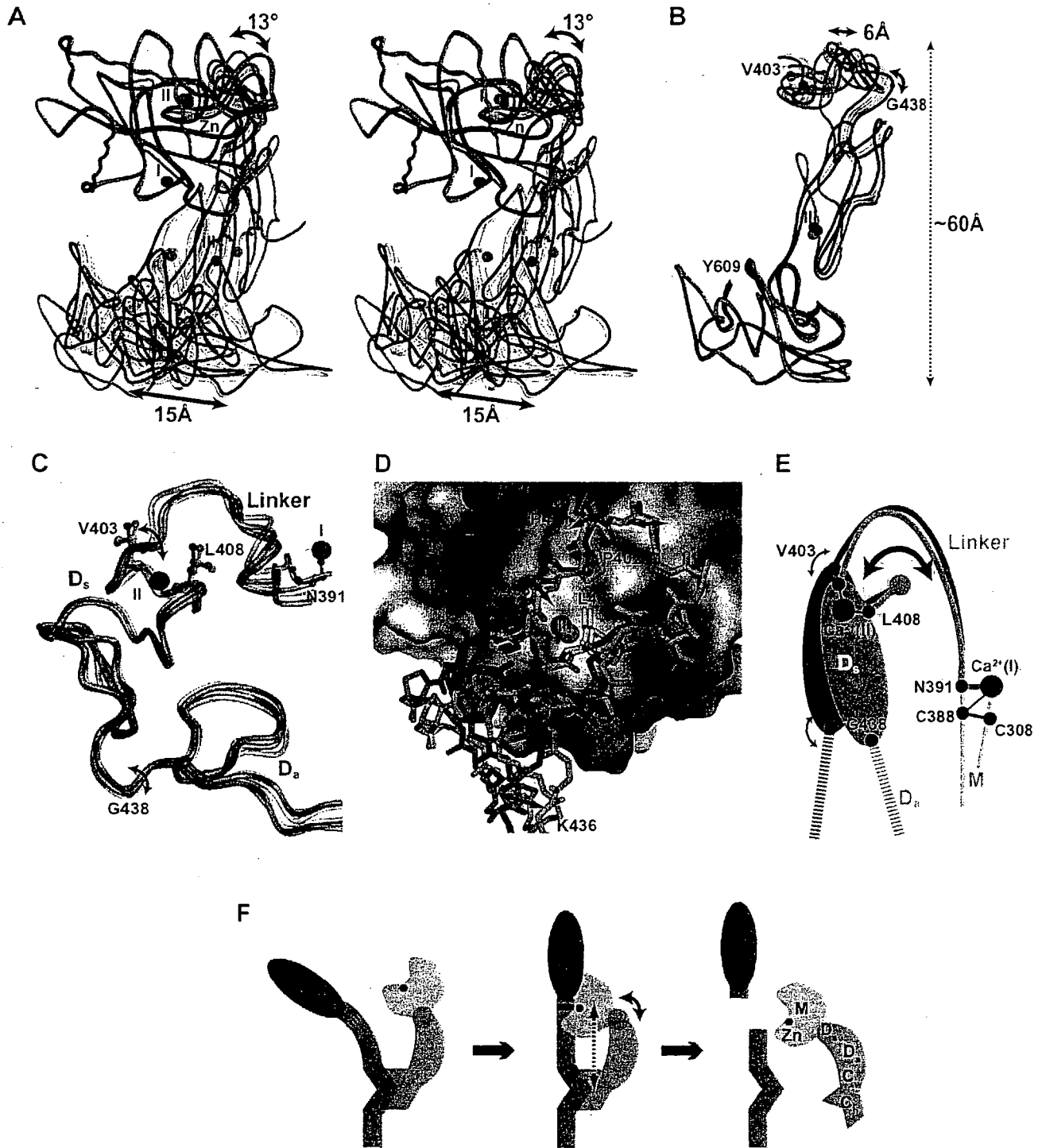


Fig. 3. Mobility of the sub-domains. (A) The M-domains of the six catrocollastatin/VAP2B molecules and the VAP1 monomer were superimposed and are shown in stereo. Two representative catrocollastatin/VAP2B molecules are shown in blue and red, the other four catrocollastatin/VAP2B molecules are in gray, and the VAP1 monomer is in green. The zinc ion is shown as a yellow sphere. The calcium atoms bound to the red and blue catrocollastatin/VAP2B molecule and VAP1 are shown as red, blue and green spheres, respectively. Superimposition of the D_h and C_s segments of the six catrocollastatin/VAP2B molecules and the VAP1 monomer are shown in B and C, respectively. (D) Close-up view of the shoulder joint. The molecular surface of the M-domain is colored according to the electrochemical surface potential (red to blue). The linker and part of the D_s segment of the two representative catrocollastatin/VAP2B molecules are shown as stick representations in pink and cyan, respectively. (E) Schematic diagram of the hinge motion at the shoulder joint. (F) Schematic model of substrate recognition and cleavage by a soluble ADAM/adamalysin/reprolysin protein.

generation of disintegrins with different lengths. Fertilin α (ADAM1) and β (ADAM2) undergo proteolytic processing within Ca^{2+} -binding site III and the linker region, respectively

at different stages of sperm maturation (Fig. 4, Supplementary Fig. 1) [36,37]. The current structural data suggests that Ca^{2+} -binding, together with a flexible modular structure, may also

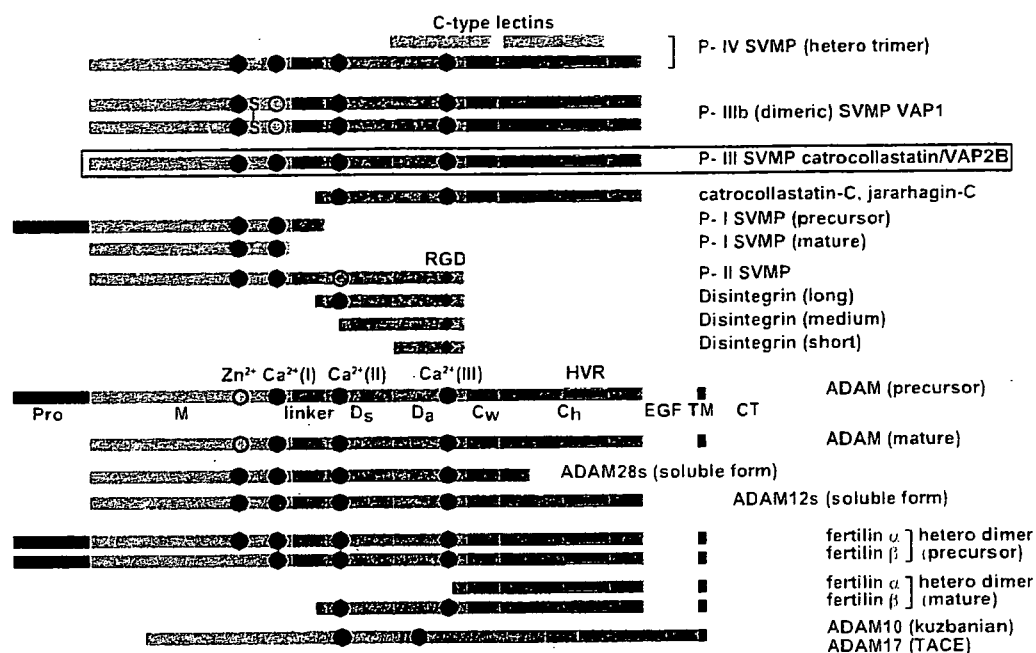


Fig. 4. Schematic representation of the modular architecture of ADAM/adamalysin/reprolysin family proteins. Each sub-domain is colored as for Fig. 1; the pro-domain (Pro), EGF-like domain (EGF), transmembrane region (TM) and cytoplasmic domain (CT) are in black, yellow, black and light salmon, respectively. The RGD sequences in disintegrins and an interchain disulfide bond in VAP1 are indicated. The Zn²⁺ and Ca²⁺ ions are shown as red and black circles, respectively; the closed circles indicate that all the members have a complete metal-binding sequence, whereas, open circles indicate that some members do not have it.

play a role in differential proteolytic processing of precursor proteins, giving rise to the biochemical and functional complexity of Crotalid and Viperid snake venoms, as well as post-translational regulation of ADAMs' functions.

4. Conclusion

ADAMs are widely distributed and constitute major membrane-bound sheddases that proteolytically process cell-surface-proteins for cell–cell communication. As such, they have emerged as potential therapeutic targets for a variety of diseases. SVMPs are key toxins involved in venom-induced pathogenesis, and thus are important targets for antivenom therapeutics. However, the physiological targets of ADAMs and SVMPs, and the molecular mechanism of target recognition are poorly understood. The structures presented here reveal a dynamic, modular architecture of the MDC domains of ADAM/adamalysin/reprolysin family proteins. Intrinsic flexibility may be important for fine-tuning substrate recognition, adjusting the spatial alignment of the catalytic and adhesion sites, and for post-translational regulation of this family of proteins.

Acknowledgement: We thank M. Tomisako for her help in crystallization experiments. This work was partly supported by Grant nano-001 for Research on Advanced Medical Technology from the Ministry of Health, Labor, and Welfare of Japan, and by grants from the Takeda Science Foundation, from the Kao Foundation for Arts and Science, from Mitsubishi Pharma Research Foundation and from Senri Life Science Foundation. T. I is supported by the grant from New Energy and Industrial Technology Development Organization (NEDO) of Japan.

Appendix A. Supplementary data

The atomic coordinates and structure factors have been deposited in the Protein Data Bank under accession codes 2DW0, 2DW1 and 2DW2 for the Form 2-1, Form 2-2 and Form 2-5 crystals, respectively. Supplementary data associated with this article can be found, in the online version, at doi:10.1016/j.febslet.2007.04.057.

References

- [1] Gutierrez, J.M., Rucavado, A., Escalante, T. and Diaz, C. (2005) Hemorrhage induced by snake venom metalloproteinases: biochemical and biophysical mechanisms involved in microvessel damage. *Toxicon* 45, 997–1011.
- [2] Araki, S., Ishida, T., Yamamoto, T., Kaji, K. and Hayashi, H. (1993) Induction of apoptosis by hemorrhagic snake venom in vascular endothelial cells. *Biochem. Biophys. Res. Commun.* 190, 148–153.
- [3] Masuda, S., Araki, S., Yamamoto, T., Kaji, K. and Hayashi, H. (1997) Purification of a vascular apoptosis-inducing factor from hemorrhagic snake venom. *Biochem. Biophys. Res. Commun.* 235, 59–63.
- [4] Masuda, S., Hayashi, H. and Araki, S. (1998) Two vascular apoptosis-inducing proteins from snake venom are members of the metalloprotease/disintegrin family. *Eur. J. Biochem.* 253, 36–41.
- [5] Trummel, K. et al. (2005) A novel metalloprotease from *Vipera lebetina* venom induces human endothelial cell apoptosis. *Toxicon* 46, 46–61.
- [6] Masuda, S., Hayashi, H., Atoda, H., Morita, T. and Araki, S. (2001) Purification, cDNA cloning and characterization of the vascular apoptosis-inducing protein, HV1, from *Trimeresurus flavoviridis*. *Eur. J. Biochem.* 268, 3339–3345.
- [7] You, W.K., Seo, H.J., Chung, K.H. and Kim, D.S. (2003) A novel metalloprotease from *Gloydius halys* venom induces endothelial

- cell apoptosis through its protease and disintegrin-like domains. *J. Biochem. (Tokyo)* 134, 739–749.
- [8] Masuda, S., Ohta, T., Kaji, K., Fox, J.W., Hayashi, H. and Araki, S. (2000) cDNA cloning and characterization of vascular apoptosis-inducing protein 1. *Biochem. Biophys. Res. Commun.* 278, 197–204.
- [9] Bjarnason, J.B. and Fox, J.W. (1995) Snake venom metalloendopeptidases: reprotolysins. *Meth. Enzymol.* 248, 345–368.
- [10] Fox, J.W. and Serrano, S.M. (2005) Structural considerations of the snake venom metalloproteinases, key members of the M12 reprotolysin family of metalloproteinases. *Toxicon* 45, 969–985.
- [11] Araki, S., Masuda, S., Maeda, H., Ying, M.J. and Hayashi, H. (2002) Involvement of specific integrins in apoptosis induced by vascular apoptosis-inducing protein 1. *Toxicon* 40, 535–542.
- [12] Maruyama, J., Hayashi, H., Miao, J., Sawada, H. and Araki, S. (2005) Severe cell fragmentation in the endothelial cell apoptosis induced by snake apoptosis toxin VAP1 is an apoptotic characteristic controlled by caspases. *Toxicon* 46, 1–6.
- [13] Seals, D.F. and Courtneidge, S.A. (2003) The ADAMs family of metalloproteases: multidomain proteins with multiple functions. *Genes Dev.* 17, 7–30.
- [14] White, J.M. (2003) ADAMs: modulators of cell–cell and cell–matrix interactions. *Curr. Opin. Cell Biol.* 15, 598–606.
- [15] Gomis-Ruth, F.X., Kress, L.F. and Bode, W. (1993) First structure of a snake venom metalloproteinase: a prototype for matrix metalloproteinases/collagenases. *EMBO J.* 12, 4151–4157.
- [16] Maskos, K. et al. (1998) Crystal structure of the catalytic domain of human tumor necrosis factor- α -converting enzyme. *Proc. Natl. Acad. Sci. USA* 95, 3408–3412.
- [17] Orth, P. et al. (2004) Crystal structure of the catalytic domain of human ADAM33. *J. Mol. Biol.* 335, 129–137.
- [18] Janes, P.W. et al. (2005) Adam meets Eph: an ADAM substrate recognition module acts as a molecular switch for ephrin cleavage in trans. *Cell* 123, 291–304.
- [19] Takeda, S., Igarashi, T., Mori, H. and Araki, S. (2006) Crystal structures of VAP1 reveal ADAMs' MDC domain architecture and its unique C-shaped scaffold. *EMBO J.* 25, 2388–2396.
- [20] Zhou, Q., Smith, J.B. and Grossman, M.H. (1995) Molecular cloning and expression of catrocollastatin, a snake-venom protein from *Crotalus atrox* (western diamondback rattlesnake) which inhibits platelet adhesion to collagen. *Biochem. J.* 307 (Pt 2), 411–417.
- [21] Igarashi, T., Oishi, Y., Araki, S., Mori, H. and Takeda, S. (2006) Crystallization and preliminary X-ray crystallographic analysis of two vascular apoptosis-inducing proteins (VAPs) from *Crotalus atrox* venom. *Acta Crystallogr. Sect. F Struct. Biol. Cryst. Commun.* 62, 688–691.
- [22] Otwinoski, Z. and Minor, W. (1997) in: *Methods in Enzymology* (Carter, C.W. and Sweet, R.M., Eds.), vol. 276, pp. 307–325.
- [23] CCP4. (1994) The CCP4 suite: programs for protein crystallography. *Acta Crystallogr. D Biol. Crystallogr.* 50, 760–763.
- [24] Roussel, A. and Cambillau, C. (1996) AFMB-CNRS, Marseille, France.
- [25] Brunger, A.T. et al. (1998) Crystallography & NMR system: a new software suite for macromolecular structure determination. *Acta Crystallogr. D Biol. Crystallogr.* 54 (Pt 5), 905–921.
- [26] Kraulis, P.J. (1991) MOLSCRIPT: a program to produce both detailed and schematic plots of protein structure. *Acta Crystallogr. D Biol. Crystallogr.* 24, 946–950.
- [27] Merritt, E.A.A.B. and David, J. (1997) in: *Methods in Enzymology*, vol. 277, pp. 505–524.
- [28] DeLano, W.L. (2002) DeLano Scientific, San Carlos, CA, USA.
- [29] Masuda, S., Maeda, H., Miao, J.Y., Hayashi, H. and Araki, S.-C. (2007) cDNA cloning and some additional peptide characterization of a single-chain vascular apoptosis-inducing protein, VAP2. *Endothelium* 14, 1–8.
- [30] Bode, W., Gomis-Ruth, F.X. and Stockler, W. (1993) Astacins, serralysins, snake venom and matrix metalloproteinases exhibit identical zinc-binding environments (HEXXHXXGXXH and Met-turn) and topologies and should be grouped into a common family, the 'metzincins'. *FEBS Lett.* 331, 134–140.
- [31] Gomis-Ruth, F.X. (2003) Structural aspects of the metzincin clan of metalloendopeptidases. *Mol. Biotechnol.* 24, 157–202.
- [32] Kini, R.M. and Evans, H.J. (1992) Structural domains in venom proteins: evidence that metalloproteinases and non-enzymatic platelet aggregation inhibitors (disintegrins) from snake venoms are derived by proteolysis from a common precursor. *Toxicon* 30, 265–293.
- [33] Calvete, J.J., Marcinkiewicz, C., Monleon, D., Esteve, V., Celda, B., Juarez, P. and Sanz, L. (2005) Snake venom disintegrins: evolution of structure and function. *Toxicon* 45, 1063–1074.
- [34] Takeya, H., Nishida, S., Nishino, N., Makinose, Y., Omori-Satoh, T., Nikai, T., Sugihara, H. and Iwanaga, S. (1993) Primary structures of platelet aggregation inhibitors (disintegrins) auto-protolytically released from snake venom hemorrhagic metalloproteinases and new fluorogenic peptide substrates for these enzymes. *J. Biochem. (Tokyo)* 113, 473–483.
- [35] Fox, J.W. and Bjarnason, J.B. (1995) Atrolsins: metalloproteinases from *Crotalus atrox* venom. *Meth. Enzymol.* 248, 368–387.
- [36] Blobel, C.P., Myles, D.G., Primakoff, P. and White, J.M. (1990) Proteolytic processing of a protein involved in sperm-egg fusion correlates with acquisition of fertilization competence. *J. Cell Biol.* 111, 69–78.
- [37] Blobel, C.P., Wolfsberg, T.G., Turck, C.W., Myles, D.G., Primakoff, P. and White, J.M. (1992) A potential fusion peptide and an integrin ligand domain in a protein active in sperm-egg fusion. *Nature* 356, 248–252.

Hypothermia reduces ischemia- and stimulation-induced myocardial interstitial norepinephrine and acetylcholine releases

Toru Kawada,¹ Hirotohi Kitagawa,² Toji Yamazaki,² Tsuyoshi Akiyama,² Atsunori Kamiya,¹ Kazunori Uemura,¹ Hidezo Mori,² and Masaru Sugimachi¹

¹Department of Cardiovascular Dynamics, Advanced Medical Engineering Center, and

²Department of Cardiac Physiology, National Cardiovascular Center Research Institute, Osaka, Japan

Submitted 4 June 2006; accepted in final form 1 November 2006

Kawada T, Kitagawa H, Yamazaki T, Akiyama T, Kamiya A, Uemura K, Mori H, Sugimachi M. Hypothermia reduces ischemia- and stimulation-induced myocardial interstitial norepinephrine and acetylcholine releases. *J Appl Physiol* 102: 622–627, 2007. First published November 2, 2006; doi:10.1152/jappphysiol.00622.2006.—Although hypothermia is one of the most powerful modulators that can reduce ischemic injury, the effects of hypothermia on the function of the cardiac autonomic nerves in vivo are not well understood. We examined the effects of hypothermia on the myocardial interstitial norepinephrine (NE) and ACh releases in response to acute myocardial ischemia and to efferent sympathetic or vagal nerve stimulation in anesthetized cats. We induced acute myocardial ischemia by coronary artery occlusion. Compared with normothermia ($n = 8$), hypothermia at 33°C ($n = 6$) suppressed the ischemia-induced NE release [63 nM (SD 39) vs. 18 nM (SD 25), $P < 0.01$] and ACh release [11.6 nM (SD 7.6) vs. 2.4 nM (SD 1.3), $P < 0.01$] in the ischemic region. Under hypothermia, the coronary occlusion increased the ACh level from 0.67 nM (SD 0.44) to 6.0 nM (SD 6.0) ($P < 0.05$) and decreased the NE level from 0.63 nM (SD 0.19) to 0.40 nM (SD 0.25) ($P < 0.05$) in the nonischemic region. Hypothermia attenuated the nerve stimulation-induced NE release from 1.05 nM (SD 0.85) to 0.73 nM (SD 0.73) ($P < 0.05$, $n = 6$) and ACh release from 10.2 nM (SD 5.1) to 7.1 nM (SD 3.4) ($P < 0.05$, $n = 5$). In conclusion, hypothermia attenuated the ischemia-induced NE and ACh releases in the ischemic region. Moreover, hypothermia also attenuated the nerve stimulation-induced NE and ACh releases. The Bezold-Jarisch reflex evoked by the left anterior descending coronary artery occlusion, however, did not appear to be affected under hypothermia.

vagal nerve; sympathetic nerve; cardiac microdialysis; cats

HYPOTHERMIA IS ONE OF THE most powerful modulators that can reduce ischemic injury in the central nervous system, heart, and other organs. The general consensus is that hypothermia induces a hypometabolic state in tissues and balances energy supply and demand (25). With respect to the myocardial ischemia, the size of a myocardial infarction correlates with temperature (6), and mild hypothermia can protect the myocardium against acute ischemic injury (9). The effects of hypothermia on the function of the cardiac autonomic nerves in terms of neurotransmitter releases, however, are not fully understood. Because autonomic neurotransmitters such as norepinephrine (NE) and ACh directly impinge on the myocardium, they would be implicated in the cardioprotection by hypothermia.

In previous studies from our laboratory, Kitagawa et al. (16) demonstrated that hypothermia attenuated the nonexocytotic NE release induced pharmacologically by ouabain, tyramine, or cyanide. Kitagawa et al. (15) also demonstrated that hypothermia attenuated the exocytotic NE release in response to vena cava occlusion or to local administration of high K^+ . The effects of hypothermia on the ischemia-induced myocardial interstitial NE release, however, were not examined in those studies. In addition, the effects of hypothermia on the ischemia-induced myocardial interstitial ACh release have never been examined. Because both sympathetic and parasympathetic nerves control the heart, simultaneous monitoring of the myocardial interstitial releases of NE and ACh (14, 31) would help integrative understanding of the autonomic nerve terminal function under hypothermia in conjunction with acute myocardial ischemia.

In the present study, the effects of hypothermia on the ischemia-induced and nerve stimulation-induced myocardial interstitial neurotransmitter releases were examined. We implanted a dialysis probe into the left ventricular free wall of anesthetized cats and measured dialysate NE and ACh levels as indexes of neurotransmitter outputs from the cardiac sympathetic and vagal nerve terminals, respectively. Based on our laboratory's previous results (15, 16), we hypothesized that hypothermia would attenuate the neurotransmitter releases in response to acute myocardial ischemia and to electrical nerve stimulation.

MATERIALS AND METHODS

Surgical Preparation and Protocols

Animals were cared for in accordance with the *Guiding Principles for the Care and Use of Animals in the Field of Physiological Sciences*, approved by the Physiological Society of Japan. All protocols were reviewed and approved by the Animal Subjects Committee of National Cardiovascular Center. Adult cats were anesthetized via an intraperitoneal injection of pentobarbital sodium (30–35 mg/kg) and ventilated mechanically through an endotracheal tube with oxygen-enriched room air. The level of anesthesia was maintained with a continuous intravenous infusion of pentobarbital sodium ($1-2 \text{ mg}\cdot\text{kg}^{-1}\cdot\text{h}^{-1}$) through a catheter inserted from the right femoral vein. Mean arterial pressure (MAP) was measured using a pressure transducer connected to a catheter inserted from the right femoral artery. Heart rate (HR) was determined from an electrocardiogram.

Protocol 1: acute myocardial ischemia. We examined the effects of hypothermia on the ischemia-induced myocardial interstitial releases of NE and ACh. The heart was exposed by partially removing the left fifth and/or sixth rib. A dialysis probe was implanted transversely into

Address for reprint requests and other correspondence: T. Kawada, Dept. of Cardiovascular Dynamics, Advanced Medical Engineering Center, National Cardiovascular Center Research Institute, 5-7-1 Fujishirodai, Suita, Osaka 565-8565, Japan (e-mail: torukawa@res.ncvc.go.jp).

The costs of publication of this article were defrayed in part by the payment of page charges. The article must therefore be hereby marked "advertisement" in accordance with 18 U.S.C. Section 1734 solely to indicate this fact.

the anterolateral free wall of the left ventricle perfused by the left anterior descending coronary artery (LAD) to monitor myocardial interstitial NE and ACh levels in the ischemic region during occlusion of the LAD (13). Another dialysis probe was implanted transversely into the posterior free wall of the left ventricle perfused by the left circumflex coronary artery to monitor myocardial interstitial NE and ACh levels in a nonischemic region. Heparin sodium (100 U/kg) was administered intravenously to prevent blood coagulation. Animals were divided into a normothermic group ($n = 8$) and a hypothermic group ($n = 6$). In the hypothermic group, surface cooling with ice bags was performed until the esophageal temperature decreased to 33°C (15, 16). A stable hypothermic condition was obtained within ~2 h. In each group, we occluded the LAD for 60 min and examined changes in the myocardial interstitial NE and ACh levels in the ischemic region (i.e., the LAD region) and nonischemic region (i.e., the left circumflex coronary artery region). Fifteen-minute dialysate samples were obtained during the preocclusion baseline condition and during the periods of 0–15, 15–30, 30–45, and 45–60 min of the LAD occlusion.

Protocol 2: sympathetic stimulation. We examined the effects of hypothermia on the sympathetic nerve stimulation-induced myocardial interstitial NE release ($n = 6$). A dialysis probe was implanted transversely into the anterolateral free wall of the left ventricle. The bilateral cardiac sympathetic nerves originating from the stellate ganglia were exposed through a second intercostal space and sectioned. The cardiac end of each sectioned nerve was placed on a bipolar platinum electrode for sympathetic stimulation (5 Hz, 10 V, 1-ms pulse duration). The electrodes and nerves were covered with mineral oil to provide insulation and prevent desiccation. A 4-min dialysate sample was obtained during the sympathetic stimulation under the normothermic condition. Thereafter, hypothermia was introduced using the same cooling procedure as in *protocol 1*, and a second 4-min dialysate sample was obtained during the sympathetic stimulation.

Protocol 3: vagal stimulation. We examined the effects of hypothermia on the vagal nerve stimulation-induced ACh release ($n = 5$). A dialysis probe was implanted transversely into the anterolateral free wall of the left ventricle. The bilateral vagi were exposed through a midline cervical incision and sectioned at the neck. The cardiac end of each sectioned nerve was placed on a bipolar platinum electrode for vagal stimulation (20 Hz, 10 V, 1-ms pulse duration). To prevent severe bradycardia and cardiac arrest, which can be induced by the vagal stimulation, the heart was paced at 200 beats/min using pacing wires attached to the apex of the heart during the stimulation period. A 4-min dialysate sample was obtained during the vagal stimulation under the normothermic condition. Thereafter, hypothermia was introduced using the same cooling procedure as in *protocol 1*, and a second 4-min dialysate sample was obtained during the vagal stimulation.

Because of the relatively intense stimulation of the sympathetic or vagal nerve, the stimulation period in *protocols 2* and *3* was limited to 4 min to minimize gradual waning of the stimulation effects. At the end of the experiment, the animals were killed by increasing the depth of anesthesia with an overdose of pentobarbital sodium. We then confirmed that the dialysis probes had been threaded in the middle layer of the left ventricular myocardium.

Dialysis Technique

The dialysate NE and ACh concentrations were measured as indexes of myocardial interstitial NE and ACh levels, respectively. The materials and properties of the dialysis probe have been described previously (2, 3). Briefly, we designed a transverse dialysis probe. A dialysis fiber (13-mm length, 310- μ m outer diameter, 200- μ m inner diameter; PAN-1200, 50,000 molecular weight cutoff; Asahi Chemical) was connected at both ends to polyethylene tubes (25-cm length, 500- μ m outer diameter, 200- μ m inner diameter). The dialysis probe

was perfused with Ringer solution containing a cholinesterase inhibitor eserine (10^{-4} M) at a rate of 2 μ l/min. We started dialysate sampling from 2 h after the implantation of the dialysis probe(s), when the dialysate NE and ACh concentrations had reached steady states. The actual dialysate sampling was delayed by 5 min from the collection period to account for the dead space volume between the semipermeable membrane and the sample tube. Each sample was collected in a microtube containing 3 μ l of HCl to prevent amine oxidation. The dialysate ACh concentration was measured directly by HPLC with electrochemical detection (Eicom). The in vitro recovery rate of ACh was ~70%. With the use of a criterion of signal-to-noise ratio of higher than three, the detection limit for ACh was 3 pg per injection. The dialysate NE concentration was measured by another HPLC-electrochemical detection system after the removal of interfering compounds by an alumina procedure. The in vitro recovery rate of NE was ~55%. With the use of a criterion of signal-to-noise ratio of higher than three, the detection limit for NE was 200 fg per injection.

Statistical Analysis

All data are presented as means and SD values. For *protocol 1*, we performed two-way repeated-measures ANOVA using hypothermia as one factor and the dialysate sampling periods (the effects of ischemia) as the other factor. For *protocols 2* and *3*, we compared stimulation-induced releases of NE and ACh before and during hypothermia using a paired *t*-test. For all of the statistics, the difference was considered significant when $P < 0.05$.

RESULTS

Figure 1A illustrates changes in myocardial interstitial NE levels in the ischemic region during LAD occlusion obtained from *protocol 1*. The inset shows the magnified ordinate for the

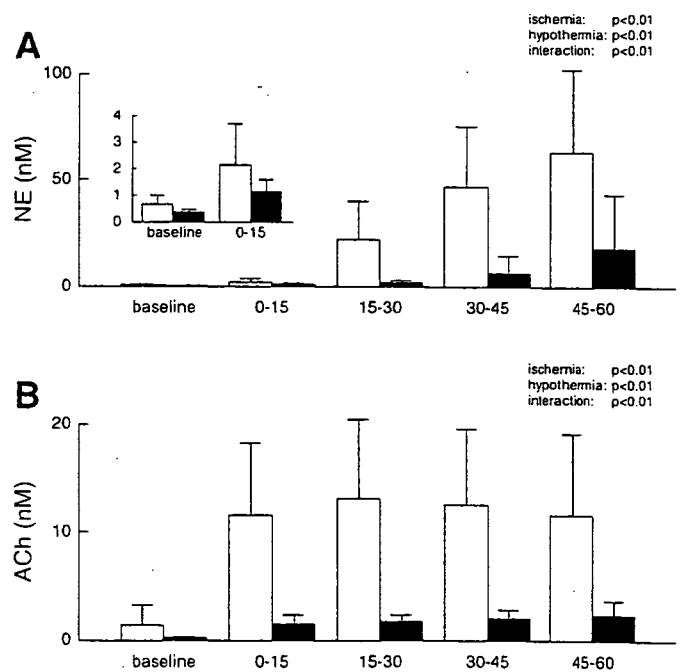


Fig. 1. A: ischemia-induced myocardial interstitial norepinephrine (NE) release in the ischemic region. Acute myocardial ischemia caused a progressive increase in the level of myocardial interstitial NE. Hypothermia attenuated the ischemia-induced NE release. Inset: magnified ordinate for the baseline and the 0- to 15-min period of ischemia. B: ischemia-induced myocardial interstitial ACh release in the ischemic region. Acute myocardial ischemia increased the myocardial interstitial ACh levels. Hypothermia attenuated the ischemia-induced ACh release. Open bars: normothermia; solid bars: hypothermia.

baseline and the 0- to 15-min period of ischemia. In the normothermic group (open bars), the LAD occlusion caused an ~94-fold increase in the NE level during the 45- to 60-min interval. In the hypothermic group (solid bars), the LAD occlusion caused an ~45-fold increase in the NE level during the 45- to 60-min interval. Compared with normothermia, hypothermia suppressed the baseline NE level to ~59% and the NE level during the 45- to 60-min period to ~29%. Statistical analysis indicated that the effects of both hypothermia and ischemia on the NE release were significant, and the interaction between hypothermia and ischemia was also significant.

Figure 1B illustrates changes in myocardial interstitial ACh levels in the ischemic region during the LAD occlusion. In both the normothermic (open bars) and hypothermic (solid bars) groups, the LAD occlusion caused an approximately eightfold increase in the ACh level during the 45- to 60-min interval. Compared with normothermia, however, hypothermia suppressed both the baseline ACh level and the ACh level during the 45- to 60-min period of ischemia to ~20%. Statistical analysis indicated that the effects of both hypothermia and ischemia on the ACh release were significant, and the interaction between hypothermia and ischemia was also significant.

Figure 2A illustrates changes in myocardial interstitial NE levels in the nonischemic region during the LAD occlusion. Note that scale of the ordinate is only one-hundredth of that in Fig. 1A. The LAD occlusion decreased the NE level in the normothermic group (open bars); the NE level during the 45- to 60-min interval was ~59% of the baseline level. The LAD occlusion also decreased the NE level in the hypothermic

Table 1. Mean arterial pressure during acute myocardial ischemia obtained in protocol 1

| | Baseline | 5 min | 15 min | 30 min | 45 min | 60 min |
|--------------|----------|----------|----------|----------|----------|----------|
| Normothermia | 108 (23) | 102 (28) | 101 (24) | 101 (20) | 102 (21) | 102 (21) |
| Hypothermia | 108 (11) | 80 (17) | 87 (10) | 85 (10) | 86 (10) | 91 (11) |

Values are means (SD) (in mmHg) obtained during preocclusion baseline period and 5-, 15-, 30-, 45-, and 60-min periods of coronary artery occlusion. Ischemia: $P < 0.01$; hypothermia: not significant; interaction: $P < 0.01$.

group (solid bars); the NE level during the 45- to 60-min interval was ~64% of the baseline level. Although the LAD occlusion resulted in a decrease in the NE level under both conditions, the NE level under hypothermia was nearly twice that measured under normothermia. The statistical analysis indicated that the effects of both hypothermia and ischemia on the NE release were significant, whereas the interaction between hypothermia and ischemia was not significant.

Figure 2B illustrates changes in myocardial interstitial ACh levels in the nonischemic region during the LAD occlusion. The LAD occlusion caused an ~3.4-fold increase in the ACh level during the 0- to 15-min interval in the normothermic group (open bars). The LAD occlusion caused an approximately ninefold increase in the ACh level during the 0- to 15-min interval in the hypothermic group (solid bars). These effects of ischemia on the ACh release were statistically significant. Although hypothermia seemed to attenuate the baseline ACh level, the overall effects of hypothermia on the ACh level were insignificant.

Tables 1 and 2 summarize the MAP and HR data, respectively, obtained in protocol 1. Acute myocardial ischemia significantly reduced MAP ($P < 0.01$) and HR ($P < 0.01$). Hypothermia did not affect MAP but did decrease HR ($P < 0.01$). The interaction between ischemia and hypothermia was significant for MAP but not for HR by the two-way repeated-measures ANOVA.

For protocol 2, hypothermia significantly attenuated the sympathetic stimulation-induced NE release to ~70% of the level observed during normothermia (Fig. 3A). Under normothermia, the sympathetic stimulation increased MAP from 114 mmHg (SD 27) to 134 mmHg (SD 33) ($P < 0.01$) and HR from 147 beats/min (SD 9) to 207 beats/min (SD 5) ($P < 0.01$). Under hypothermia, the sympathetic stimulation increased MAP from 117 mmHg (SD 11) to 136 mmHg (SD 22) ($P < 0.05$) and HR from 125 beats/min (SD 16) to 164 beats/min (SD 10) ($P < 0.01$).

For protocol 3, hypothermia significantly attenuated the vagal stimulation-induced ACh release to ~70% of the level observed during normothermia (Fig. 3B). Hypothermia did not change MAP [117 mmHg (SD 18) vs. 118 mmHg (SD 27)] but

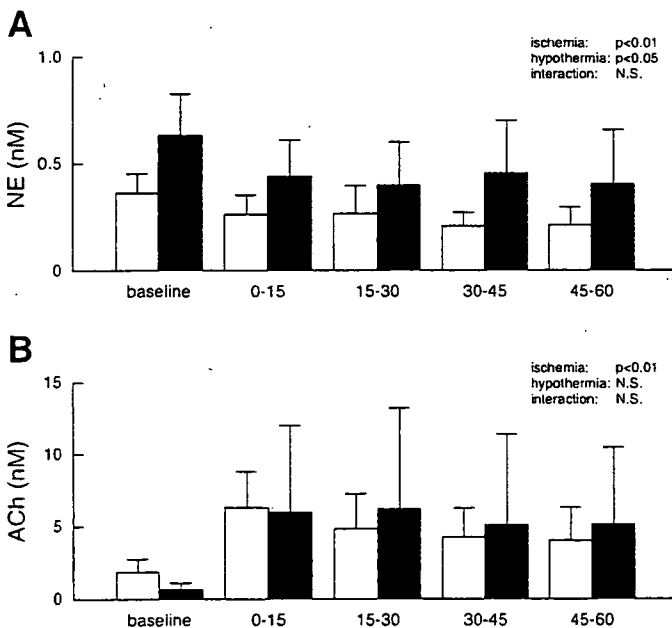


Fig. 2. A: changes in the myocardial interstitial NE levels in the nonischemic region. Acute myocardial ischemia decreased the level of myocardial interstitial NE from the baseline level. Hypothermia increased the myocardial interstitial NE levels in the nonischemic region. B: changes in the myocardial interstitial ACh levels in the nonischemic region. Acute myocardial ischemia increased the myocardial interstitial ACh level. Hypothermia did not attenuate the increasing response of ACh to the left anterior descending coronary artery occlusion. Open bars: normothermia; solid bars: hypothermia. NS, not significant.

Table 2. Heart rate during acute myocardial ischemia obtained in protocol 1

| | Baseline | 5 min | 15 min | 30 min | 45 min | 60 min |
|--------------|----------|----------|----------|----------|----------|----------|
| Normothermia | 183 (26) | 160 (18) | 163 (16) | 163 (18) | 166 (20) | 165 (21) |
| Hypothermia | 146 (25) | 116 (19) | 113 (19) | 126 (39) | 112 (20) | 97 (31) |

Values are means (SD) (in beats/min) obtained during preocclusion baseline period and 5-, 15-, 30-, 45-, and 60-min periods of coronary artery occlusion. Ischemia: $P < 0.01$; hypothermia: $P < 0.01$; interaction: not significant.

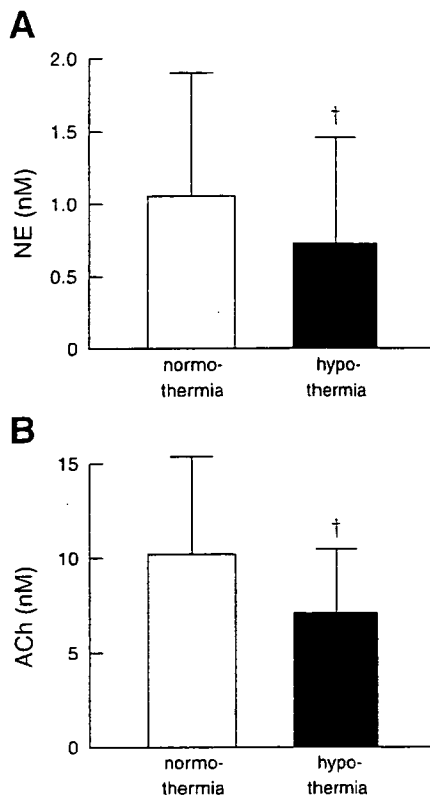


Fig. 3. *A*: efferent sympathetic nerve stimulation-induced release of myocardial interstitial NE before and during hypothermia. †Hypothermia significantly attenuated the stimulation-induced NE release. *B*: efferent vagal nerve stimulation-induced release of myocardial interstitial ACh before and during hypothermia. †Hypothermia significantly attenuated the stimulation-induced ACh release.

did decrease HR from 202 beats/min (SD 24) to 179 beats/min (SD 15) ($P < 0.05$) during the prestimulation, unpaced condition. MAP during the stimulation was 105 mmHg (SD 19) under normothermia and 93 mmHg (SD 33) under hypothermia.

DISCUSSION

A cardiac microdialysis is a powerful tool to estimate neurotransmitter levels in the myocardial interstitium *in vivo* (2, 3, 14, 19, 20, 31). The present study demonstrated that hypothermia significantly attenuated the myocardial interstitial releases of NE and ACh in the ischemic region during the LAD occlusion. In contrast, the increasing response in the ACh level from its baseline level and the decreasing response in the NE level from its baseline level observed in the nonischemic region were maintained under hypothermia. To our knowledge, this is the first report showing the effects of hypothermia on the myocardial interstitial releases of NE and ACh during acute myocardial ischemia *in vivo*. In addition, the present study showed that hypothermia significantly attenuated nerve stimulation-induced myocardial interstitial NE and ACh releases *in vivo*.

Effects of Hypothermia on Ischemia-induced NE and ACh Releases in the Ischemic Region

Acute myocardial ischemia causes energy depletion, which leads to myocardial interstitial NE release in the ischemic

region (Fig. 1A). The NE release can be classified as exocytotic or nonexocytotic (18, 24). Exocytotic release indicates NE release from synaptic vesicles, which normally occurs in response to nerve discharge and subsequent Ca^{2+} influx through voltage-dependent Ca^{2+} channels. On the other hand, nonexocytotic release indicates NE release from the axoplasm, such as that mediated by a reverse transport through the NE transporter. A neuronal uptake blocker, desipramine, can suppress the ischemia-induced NE release (19, 24). Whereas exocytotic release contributes to the ischemia-induced NE release in the initial phase of ischemia (within ~ 20 min), carrier-mediated nonexocytotic release becomes predominant as the ischemic period is prolonged (1). Hypothermia significantly attenuated the ischemia-induced NE release (Fig. 1A). The NE level during the 45- to 60-min period of ischemia under hypothermia was $\sim 20\%$ of that obtained under normothermia. The NE uptake transporter is driven by the Na^+ gradient across the cell membrane (23). The loss of the Na^+ gradient due to ischemia causes NE to be transported out of the cell by reversing the action of the NE transporter. Hypothermia inhibits the action of the NE transporter and also suppresses the intracellular Na^+ accumulation (8), thereby reducing nonexocytotic NE release during ischemia. The present results are in line with an *in vitro* study that showed hypothermia suppressed nonexocytotic NE release induced by deprivation of oxygen and glucose (30). The present results are also consistent with a previous study from our laboratory that showed hypothermia attenuated the nonexocytotic NE release induced by ouabain, tyramine, or cyanide (16).

Acute myocardial ischemia increases myocardial interstitial ACh level in the ischemic region, as reported previously (Fig. 1B) (13). The level of ischemia-induced ACh release during 0- to 15-, 15- to 30-, 30- to 45-, or 45- to 60-min period of ischemia is comparable to that evoked by 4-min electrical stimulation of the bilateral vagi (Fig. 3B). Compared with the normothermic condition, hypothermia significantly attenuated the ischemia-induced myocardial interstitial release of ACh in the ischemic region. Our laboratory's previous study indicated that intracellular Ca^{2+} mobilization is essential for the ischemia-induced release of ACh (13). Hypothermia may have prevented the Ca^{2+} overload, thereby reducing the ischemia-induced ACh release. Alternatively, hypothermia may reduce the extent of the ischemic injury, which in turn suppressed the ischemia-induced ACh release. Because ACh has protective effects on the cardiomyocytes against ischemia (11), the suppression of ischemia-induced ACh release during hypothermia itself may be unfavorable for cardioprotection.

There is considerable controversy regarding the cardioprotective effects of β -adrenergic blockade during severe ischemia, with studies demonstrating a reduction of infarct size (10, 17) or no effects (7, 27). The β -adrenergic blockade seems effective to protect the heart only when the heart is reperfused within a certain period after the coronary occlusion. The β -adrenergic blockade would reduce the myocardial oxygen consumption through the reduction of HR and ventricular contractility and delay the progression of ischemic injury. Hence the infarct size might be reduced when the heart is reperfused before the ischemic damage becomes irreversible. The ischemia-induced NE release reached nearly 100 times the baseline NE level under normothermia (Fig. 1A), which by far exceeded the NE level attained by electrical stimulation of the

bilateral stellate ganglia (Fig. 3A). Because high NE levels have cardiotoxic effects (22), ischemia-induced NE release might aggravate the ischemic injury. However, catecholamine depletion by a reserpine treatment fails to reduce the infarct size (26, 29), throwing a doubt on the involvement of catecholamine toxicity in the progression of myocardial damage during ischemia. It is, therefore, most likely that the hypothermia-induced reductions in NE and ACh are the result of reduced myocardial damage or a direct effect on nerve endings.

Van den Doel et al. (28) showed that hypothermia does not abolish necrosis, but rather delays necrosis during sustained ischemia, so that hypothermia protected against infarction produced by a 30-min occlusion but not against infarction produced by a 60-min occlusion in the rat heart. At the same time, they mentioned that hypothermia was able to reduce the infarct size after a 60-min coronary occlusion in the dog, possibly because of the significant collateral flow in the canine hearts. Because the feline hearts are similar to the canine hearts in that they have considerable collateral flow compared with the rat hearts (21), hypothermia should have protected the feline heart against the 60-min coronary occlusion in the present study.

Effects of Hypothermia on the NE and ACh Releases in the Nonischemic Region and on the Electrical Stimulation-induced NE and ACh Releases

The NE and ACh levels in the nonischemic region may reflect the sympathetic and parasympathetic drives to this region. As an example, myocardial interstitial ACh levels increase during activations of the arterial baroreflex and the Bezold-Jarisch reflex (14). In the present study, acute myocardial ischemia decreased the NE level from its baseline level, whereas it increased the ACh level from its baseline level (Fig. 2). Ischemia also decreased MAP and HR (Tables 1 and 2), suggesting that the Bezold-Jarisch reflex was induced by the LAD occlusion under both normothermia and hypothermia. Taking into account the fact that electrical stimulation-induced ACh release was attenuated to ~70% (Fig. 3), similar ACh levels during ischemia imply the enhancement of the parasympathetic outflow via the Bezold-Jarisch reflex under hypothermia. These results are in line with the study by Zheng et al. (32), where pulmonary chemoreflex-induced bradycardia was maintained under hypothermia. Hypothermia increased the NE level in the nonischemic region, suggesting that sympathetic drive to this region also increased. Hypothermic stress is known to cause sympathetic activation, accompanying increases in MAP, HR, plasma NE, and epinephrine levels (4). In the present study, because the effect of hypothermia on MAP was insignificant (Table 1) and HR decreased under hypothermia (Table 2), the sympathetic activation observed in the nonischemic region might have been regional and not systemic.

Hypothermia attenuated the releases of NE and ACh in response to respective nerve stimulation to ~70% of that observed under normothermia (Fig. 3). The suppression of the exocytotic NE release by hypothermia is consistent with a previous study from our laboratory, where hypothermia attenuated the myocardial interstitial NE release in response to vena cava occlusion or to a local high K^+ administration (15). The suppression of NE release by hypothermia is consistent with an

in vitro study by Kao and Westhead (12) in which catecholamine secretion from adrenal chromaffin cells induced by elevated K^+ levels increased as the temperature increased from 4 to 37°C. On the other hand, because hypothermia inhibits the neuronal NE uptake, the NE concentration at the synaptic cleft is expected to be increased if the level of NE release remains unchanged. Actually, Vizi (30) demonstrated that hypothermia increased NE release in response to field stimulation in vitro. In the present study, however, the suppression of NE release might have canceled the potential accumulation of NE due to NE uptake inhibition. The present study also demonstrated that the ACh release was suppressed by hypothermia. In the rat striatum, hypothermia decreases the extracellular ACh concentration and increases the choline concentration (5). Hypothermia may inhibit a choline uptake transporter in the same manner as it inhibits a NE uptake transporter. The inhibition of the choline transporter by hypothermia may have hampered the replenishment of the available pool of ACh and thereby contributed to the suppression of the stimulation-induced ACh release.

Limitations

In *protocol 1*, because we did not measure the infarct size in the present study, the degree of myocardial protection by hypothermia was undetermined. Whether the reduction of ischemia-induced neurotransmitter release correlates with the reduction of infarct size requires further investigations. In *protocols 2* and *3*, baseline NE and ACh levels were not measured. The reduction of stimulation-induced NE and ACh release by hypothermia might be partly due to the reduction of baseline NE and ACh levels. However, because transection of the stellate ganglia (31) or vagi (3) reduces the baseline NE and ACh levels, changes in the baseline NE and ACh levels by hypothermia in *protocols 2* and *3* could not be as large as those observed under innervated conditions in *protocol 1* (Figs. 1 and 2).

In conclusion, hypothermia attenuated the ischemia-induced releases of NE and ACh in the ischemic region to ~30 and 20% of those observed under normothermia, respectively. Hypothermia also attenuated the nerve stimulation-induced releases of NE and ACh to ~70% of those observed during normothermia. In contrast, hypothermia did not affect the decreasing response in the NE level and the increasing response in the ACh level in the nonischemic region, suggesting that the Bezold-Jarisch reflex evoked by the LAD occlusion was maintained.

GRANTS

This study was supported by Health and Labour Sciences Research Grant for Research on Advanced Medical Technology, Health and Labour Sciences Research Grant for Research on Medical Devices for Analyzing, Supporting and Substituting the Function of Human Body, and Health and Labour Sciences Research Grant H18-Iryo-Ippan-023 from the Ministry of Health, Labour and Welfare of Japan; Program for Promotion of Fundamental Studies in Health Science from the National Institute of Biomedical Innovation; a grant provided by the Ichiro Kanehara Foundation; Ground-based Research Announcement for Space Utilization promoted by the Japan Space Forum; and Industrial Technology Research Grant Program 03A47075 from the New Energy and Industrial Technology Development Organization of Japan.

REFERENCES

1. Akiyama T, Yamazaki T. Norepinephrine release from cardiac sympathetic nerve endings in the in vivo ischemic region. *J Cardiovasc Pharmacol* 34: S11-S14, 1999.

2. Akiyama T, Yamazaki T, Ninomiya I. In vivo monitoring of myocardial interstitial norepinephrine by dialysis technique. *Am J Physiol Heart Circ Physiol* 261: H1643-H1647, 1991.
3. Akiyama T, Yamazaki T, Ninomiya I. In vivo detection of endogenous acetylcholine release in cat ventricles. *Am J Physiol Heart Circ Physiol* 266: H854-H860, 1994.
4. Chernow B, Lake CR, Zaritsky A, Finton CK, Casey L, Rainey TG, Fletcher JR. Sympathetic nervous system "switch off" with severe hypothermia. *Crit Care Med* 11: 677-680, 1983.
5. Damsma G, Fibiger HC. The effects of anaesthesia and hypothermia on interstitial concentrations of acetylcholine and choline in rat striatum. *Life Sci* 48: 2469-2474, 1991.
6. Duncker DJ, Klassen CL, Ishibashi Y, Herrlinger SH, Pavak T, Bache R. Effect of temperature on myocardial infarction in swine. *Am J Physiol Heart Circ Physiol* 270: H1189-H1199, 1996.
7. Genth K, Hofmann M, Hofmann M, Schaper W. The effect of β -adrenergic blockade on infarct size following experimental coronary occlusion. *Basic Res Cardiol* 76: 144-151, 1981.
8. Gerevich Z, Tretter L, Adam-Vizi V, Baranyi M, Kiss JP, Zelles T, Vizi ES. Analysis of high intracellular $[Na^+]_i$ -induced release of $[^3H]$ noradrenaline in rat hippocampal slices. *Neuroscience* 104: 761-768, 2001.
9. Hale SL, Kloner RA. Myocardial temperature in acute myocardial infarction: protection with mild regional hypothermia. *Am J Physiol Heart Circ Physiol* 273: H220-H227, 1997.
10. Jang IK, Van de Werf F, Vanhaecke J, De Geest H. Coronary reperfusion by thrombolysis and early beta-adrenergic blockade in acute experimental myocardial infarction. *J Am Coll Cardiol* 14: 1816-1823, 1989.
11. Kakinuma Y, Ando M, Kuwabara M, Katare RG, Okudela K, Kobayashi M, Sato T. Acetylcholine from vagal stimulation protects cardiomyocytes against ischemia and hypoxia involving additive nonhypoxic induction of HIF-1 α . *FEBS Lett* 579: 2111-2118, 2005.
12. Kao LS, Westhead EW. Temperature dependence of catecholamine secretion from cultured bovine chromaffin cells. *J Neurochem* 43: 590-592, 1984.
13. Kawada T, Yamazaki T, Akiyama T, Sato T, Shishido T, Inagaki M, Takaki H, Sugimachi M, Sunagawa K. Differential acetylcholine release mechanisms in the ischemic and non-ischemic myocardium. *J Mol Cell Cardiol* 32: 405-414, 2000.
14. Kawada T, Yamazaki T, Akiyama T, Shishido T, Inagaki M, Uemura K, Miyamoto T, Sugimachi M, Takaki H, Sunagawa K. In vivo assessment of acetylcholine-releasing function at cardiac vagal nerve terminals. *Am J Physiol Heart Circ Physiol* 281: H139-H145, 2001.
15. Kitagawa H, Akiyama T, Yamazaki T. Effects of moderate hypothermia on in situ cardiac sympathetic nerve endings. *Neurochem Int* 40: 235-242, 2002.
16. Kitagawa H, Yamazaki T, Akiyama T, Mori H, Sunagawa K. Effects of moderate hypothermia on norepinephrine release evoked by ouabain, tyramine and cyanide. *J Cardiovasc Pharmacol* 41: S111-S114, 2003.
17. Ku DD, Lucchesi BR. Effects of dimethyl propranolol (UM-272; SC-27761) on myocardial ischemic injury in the canine heart after temporary coronary artery occlusion. *Circulation* 57: 541-548, 1978.
18. Kurz T, Richardt G, Hagl S, Seyfarth M, Schömig A. Two different mechanisms of noradrenaline release during normoxia and simulated ischemia in human cardiac tissue. *J Mol Cell Cardiol* 27: 1161-1172, 1995.
19. Lameris TW, de Zeeuw S, Alberts G, Boomsma F, Duncker DJ, Verdouw PD, Veld AJ, van den Meiracker AH. Time course and mechanism of myocardial catecholamine release during transient ischemia in vivo. *Circulation* 101: 2645-2650, 2000.
20. Lameris TW, de Zeeuw S, Duncker DJ, Alberts G, Boomsma F, Verdouw PD, van den Meiracker AH. Exogenous angiotensin II does not facilitate norepinephrine release in the heart. *Hypertension* 40: 491-497, 2002.
21. Maxwell MP, Hearse DJ, Yellon DM. Species variation in the coronary collateral circulation during regional myocardial ischaemia: a critical determinant of the rate of evolution and extent of myocardial infarction. *Cardiovasc Res* 21: 737-746, 1987.
22. Rona G. Catecholamine cardiotoxicity. *J Mol Cell Cardiol* 17: 291-306, 1985.
23. Schwartz JH. Neurotransmitters. In: *Principles of Neural Science* (4th Ed.), edited by Kandel ER, Schwartz JH, Jessell TM. New York: McGraw-Hill, 2000, p. 280-297.
24. Schömig A, Kurz T, Richardt G, Schömig E. Neuronal sodium homeostasis and axoplasmic amine concentration determine calcium-independent noradrenaline release in normoxic and ischemic rat heart. *Circ Res* 63: 214-226, 1988.
25. Simkhovich BZ, Hale SL, Kloner RA. Metabolic mechanism by which mild regional hypothermia preserves ischemic tissue. *J Cardiovasc Pharmacol Ther* 9: 83-90, 2004.
26. Toombs CF, Wiltse AL, Shebuski RJ. Ischemic preconditioning fails to limit infarct size in reserpinized rabbit myocardium. Implication of norepinephrine release in the preconditioning effect. *Circulation* 88: 2351-2358, 1993.
27. Torr S, Drake-Holland AJ, Main M, Hynd J, Isted K, Noble MIM. Effects on infarct size of reperfusion and pretreatment with β -blockade and calcium antagonists. *Basic Res Cardiol* 84: 564-582, 1989.
28. Van den Doel MA, Gho BC, Duval SY, Schoemaker RG, Duncker DJ, Verdouw PD. Hypothermia extends the cardioprotection by ischaemic preconditioning to coronary artery occlusions of longer duration. *Cardiovasc Res* 37: 76-81, 1998.
29. Vander Heide RS, Schwartz LM, Jennings RB, Reimer KA. Effect of catecholamine depletion on myocardial infarct size in dogs: role of catecholamines in ischemic preconditioning. *Cardiovasc Res* 30: 656-662, 1995.
30. Vizi ES. Different temperature dependence of carrier-mediated (cytoplasmic) and stimulus-evoked (exocytotic) release of transmitter: a simple method to separate the two types of release. *Neurochem Int* 33: 359-366, 1998.
31. Yamazaki T, Akiyama T, Kitagawa H, Takauchi Y, Kawada T, Sunagawa K. A new, concise dialysis approach to assessment of cardiac sympathetic nerve terminal abnormalities. *Am J Physiol Heart Circ Physiol* 272: H1182-H1187, 1997.
32. Zheng F, Kidd C, Bowser-Riley F. Effects of moderate hypothermia on baroreflex and pulmonary chemoreflex heart rate response in decerebrate ferrets. *Exp Physiol* 81: 409-420, 1996.

Angiotensin II attenuates myocardial interstitial acetylcholine release in response to vagal stimulation

Toru Kawada,¹ Toji Yamazaki,² Tsuyoshi Akiyama,² Meihua Li,^{1,3} Can Zheng,^{1,3} Toshiaki Shishido,¹ Hidezo Mori,² and Masaru Sugimachi¹

¹Department of Cardiovascular Dynamics, Advanced Medical Engineering Center and ²Department of Cardiac Physiology, National Cardiovascular Center Research Institute, Osaka; and ³Japan Association for the Advancement of Medical Equipment, Tokyo, Japan

Submitted 5 April 2007; accepted in final form 19 July 2007

Kawada T, Yamazaki T, Akiyama T, Li M, Zheng C, Shishido T, Mori H, Sugimachi M. Angiotensin II attenuates myocardial interstitial acetylcholine release in response to vagal stimulation. *Am J Physiol Heart Circ Physiol* 293: H2516–H2522, 2007. First published July 20, 2007; doi:10.1152/ajpheart.00424.2007.—Although ANG II exerts a variety of effects on the cardiovascular system, its effects on the peripheral parasympathetic neurotransmission have only been evaluated by changes in heart rate (an effect on the sinus node). To elucidate the effect of ANG II on the parasympathetic neurotransmission in the left ventricle, we measured myocardial interstitial ACh release in response to vagal stimulation (1 ms, 10 V, 20 Hz) using cardiac microdialysis in anesthetized cats. In a control group ($n = 6$), vagal stimulation increased the ACh level from 0.85 ± 0.03 to 10.7 ± 1.0 (SE) nM. Intravenous administration of ANG II at $10 \mu\text{g} \cdot \text{kg}^{-1} \cdot \text{h}^{-1}$ suppressed the stimulation-induced ACh release to 7.5 ± 0.6 nM ($P < 0.01$). In a group with pretreatment of intravenous ANG II receptor subtype 1 (AT₁ receptor) blocker losartan (10 mg/kg, $n = 6$), ANG II was unable to inhibit the stimulation-induced ACh release (8.6 ± 1.5 vs. 8.4 ± 1.7 nM). In contrast, in a group with local administration of losartan (10 mM, $n = 6$) through the dialysis probe, ANG II inhibited the stimulation-induced ACh release (8.0 ± 0.8 vs. 5.8 ± 1.0 nM, $P < 0.05$). In conclusion, intravenous ANG II significantly inhibited the parasympathetic neurotransmission through AT₁ receptors. The failure of local losartan administration to nullify the inhibitory effect of ANG II on the stimulation-induced ACh release indicates that the site of this inhibitory action is likely at parasympathetic ganglia rather than at postganglionic vagal nerve terminals.

cardiac microdialysis: cats; losartan

ANG II HAS a variety of effects on the cardiovascular system (22): it acts on the vascular beds to increase peripheral vascular resistance and also on the adrenal cortex to cause volume retention. These direct effects of ANG II contribute to the maintenance of arterial pressure (AP). Aside from these direct effects, ANG II has been shown to modulate the sympathetic nervous system both centrally (7, 9) and peripherally (10). With respect to the sympathetic regulation in the heart, however, exogenous ANG II does not facilitate stimulation- and ischemia-induced norepinephrine release in the porcine left ventricle (18). Compared with a number of reports on the sympathetic system, only a few reports are available as to the effects of ANG II on the parasympathetic system. In 1982, Potter (23) demonstrated that ANG II (5–10 μg iv, body wt not

reported) inhibited bradycardia induced by vagal stimulation in dogs. In that study, administration of ACh reduced the heart rate to an identical degree in the presence or absence of ANG II, suggesting that the inhibition of bradycardia by ANG II was attributable to the inhibition of the ACh release from the vagal nerve terminals. In contrast, Andrews et al. (3) reported that ANG II (500 ng/kg iv) did not inhibit bradycardia induced by vagal stimulation in ferrets. In a rat heart failure model, ANG II receptor subtype 1 (AT₁ receptor) antagonist losartan enhanced the bradycardic response to vagal stimulation (5). In pithed rats, an angiotensin-converting enzyme (ACE) inhibitor captopril also enhanced the bradycardic response to vagal stimulation (25, 26). In all of these studies, changes in the heart rate were used as a functional measurement of peripheral vagal function because of the difficulty in measuring the ACh release in the in vivo heart. Accordingly, whether ANG II affects the vagal control over the ventricle remains unknown. The aim of the present study was to examine the effect of ANG II on the vagal stimulation-induced ACh release in the left ventricular myocardium by measuring the interstitial ACh levels directly using a cardiac microdialysis technique (1, 13–15). We also explored the possible sites of action for the effect of ANG II on the stimulation-induced ACh release by administering losartan systemically from the femoral vein or locally through the dialysis fiber. Because ACh has a protective effect on the ischemic myocardium (12, 24, 29), elucidating the effect of ANG II on the ACh release in the ventricle would be helpful to understand the mechanism of ACE inhibitor or AT₁ receptor antagonist for the treatment of heart diseases (16, 17).

MATERIALS AND METHODS

Surgical Preparation

Animal care was provided in strict accordance with the *Guiding Principles for the Care and Use of Animals in the Field of Physiological Sciences* approved by the Physiological Society of Japan. All protocols were approved by the Animal Subject Committee of the National Cardiovascular Center. Twenty eight adult cats weighing from 1.9 to 4.9 kg were anesthetized using an intraperitoneal injection of pentobarbital sodium (30–35 mg/kg) and were then ventilated mechanically with room air mixed with oxygen. The depth of anesthesia was maintained by a continuous intravenous infusion of pentobarbital sodium ($1\text{--}2 \text{ mg} \cdot \text{kg}^{-1} \cdot \text{h}^{-1}$) through a catheter inserted in the right femoral vein. Systemic AP was monitored by a catheter inserted in the right femoral artery. Heart rate was determined from an

The costs of publication of this article were defrayed in part by the payment of page charges. The article must therefore be hereby marked "advertisement" in accordance with 18 U.S.C. Section 1734 solely to indicate this fact.

Address for reprint requests and other correspondence: T. Kawada, Dept. of Cardiovascular Dynamics, National Cardiovascular Center Research Institute, 5-7-1 Fujishirodai, Suita, Osaka 565-8565, Japan (e-mail: torukawa@res.nccv.go.jp).

electrocardiogram using a cardi tachometer. Esophageal temperature of the animal, measured using a thermometer (CTM-303; TERUMO), was maintained at $\sim 37^{\circ}\text{C}$ using a heating pad and a lamp. Both vagal nerves were exposed and sectioned bilaterally through a midline cervical incision. With the animal in the lateral position, we resected the left fifth and sixth ribs to approach the heart. After the incision of the pericardium, the heart was suspended in a pericardial cradle. Stainless steel wires were attached to the apex and the posterior wall of the left ventricle to pace the heart. Using a fine guiding needle, we implanted a dialysis probe transversely through the anterolateral free wall of the left ventricle. Next, we attached a pair of bipolar platinum electrodes to the cardiac end of each sectioned vagal nerve. The nerves and electrodes were covered in warmed mineral oil for insulation. We gave heparin sodium (100 U/kg) intravenously to prevent blood coagulation. At the end of the experiment, postmortem examination confirmed that the semipermeable membrane of the dialysis probe had been implanted in the left ventricular myocardium.

Dialysis Technique

The materials and properties of the dialysis probe have been described previously (1). Briefly, we designed a transverse dialysis probe in which a dialysis fiber of semipermeable membrane (13 mm length, 310 μm outer diameter, 200 μm inner diameter; PAN-1200, 50,000 mol wt cutoff; Asahi Chemical) was attached at both ends to

polyethylene tubes (25 cm length, 500 μm outer diameter, 200 μm inner diameter). The dialysis probe was perfused at a rate of 2 $\mu\text{l}/\text{min}$ with Ringer solution containing the cholinesterase inhibitor physostigmine (100 μM). Experimental protocols were started 2 h after implanting the dialysis probe when the ACh concentration in the dialysate reached a steady state. ACh concentrations in the dialysate were measured by an HPLC system with electrochemical detection (Eicom, Kyoto, Japan).

Figure 1 schematizes the three original protocols and two supplemental protocols utilized in the present study. The hatched rectangles indicate the baseline sampling, whereas the solid rectangles indicate the sampling during the 10-min vagal stimulation period (1 ms, 10 V, 20 Hz) in each protocol. The stimulus was set supramaximal to most easily delineate the possible effect of ANG II on myocardial interstitial ACh release. In all of the vagal stimulation periods, we paced the heart at 200 beats/min to avoid the difference in heart rate affecting the vagal stimulation-induced ACh release (14). For baseline sampling periods, we paced the heart at 200 beats/min when spontaneous heart rate was < 200 beats/min.

Protocol 1 ($n = 6$). We examined the effects of intravenous administration of ANG II on vagal stimulation-induced myocardial ACh release. We collected a dialysate sample under baseline conditions. We then stimulated the vagal nerve and paced the heart for 10 min and collected a dialysate sample during the stimulation period

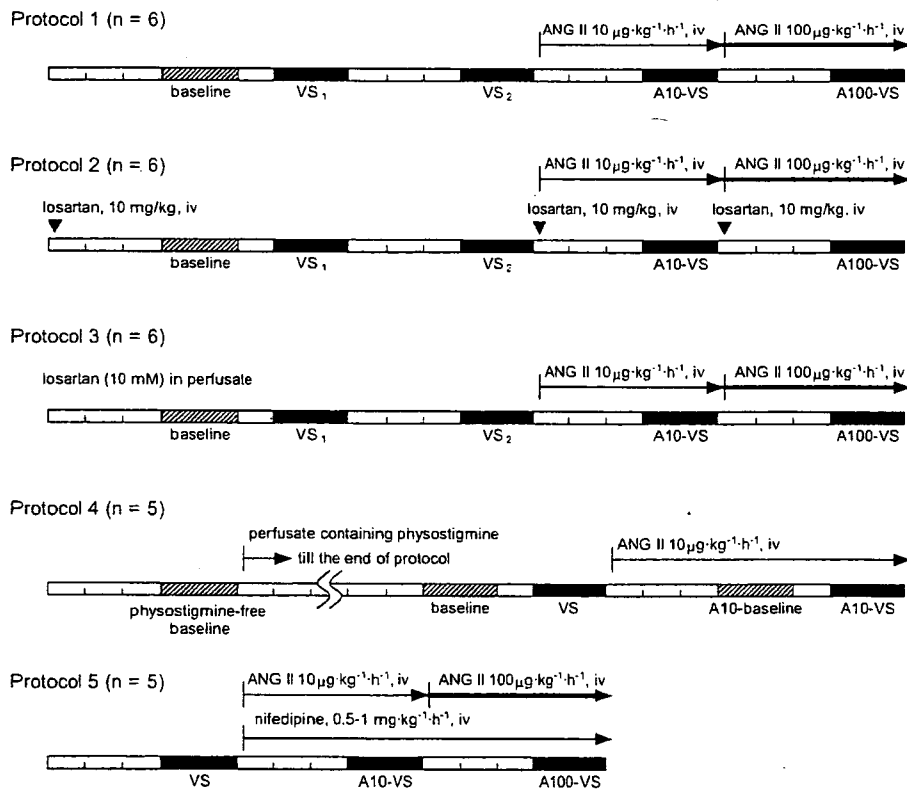


Fig. 1. Schematic representation of the protocols used in the present study. After implantation of the dialysis probe (2 h), we obtained a baseline dialysate sample (hatched rectangles) for 10 min. Thereafter, we obtained 4 dialysate samples during vagal stimulation with fixed-rate pacing for 10 min (filled rectangles) at intervening intervals of 15 min. In protocols 1 through 3, after obtaining 2 control trials (VS₁ and VS₂), we initiated intravenous administration of ANG II at 10 $\mu\text{g}\cdot\text{kg}^{-1}\cdot\text{h}^{-1}$ and waited for 15 min to obtain a dialysate sample during vagal stimulation with fixed-rate pacing (A10-VS). We then increased the dose of ANG II to 100 $\mu\text{g}\cdot\text{kg}^{-1}\cdot\text{h}^{-1}$ and waited for an additional 15 min before obtaining a dialysate sample during vagal stimulation with fixed-rate pacing (A100-VS). In protocol 2, the ANG II receptor subtype 1 blocker losartan was administered by bolus injection (10 mg/kg) before obtaining a baseline dialysate sample and also immediately before the beginning of each dose of ANG II administration (\blacktriangledown). In protocol 3, we administered losartan (10 mM) through the dialysis probe throughout the protocol. In protocol 4, we first collected a dialysate sample using perfusate free of physostigmine. We then replaced the perfusate with Ringer solution containing physostigmine and collected dialysate samples of baseline and vagal stimulation (VS). Approximately 15 min after the onset of iv ANG II administration at 10 $\mu\text{g}\cdot\text{kg}^{-1}\cdot\text{h}^{-1}$, we collected dialysate samples of baseline (A10-baseline) and vagal stimulation (A10-VS). In protocol 5, we collected dialysate samples during a control vagal stimulation (VS) and during the 2 doses of iv ANG II administration (A10-VS and A100-VS). The pressor effect of ANG II was counteracted by simultaneous iv infusion of the L-type Ca^{2+} channel blocker nifedipine.